

Water Resources Research

RESEARCH ARTICLE

10.1029/2018WR023634

Special Section:

Dynamics in Intensively Managed
Landscapes: Water, Sediment,
Nutrient, Carbon, and
Ecohydrology

Key Points:

- A process-based 3-D model is developed to simulate the coevolution of soil organic carbon (SOC) and landscape in a watershed
- Vertical SOC profiles evolve heterogeneously across the watershed due to SOC redistribution and biogeochemical transformation
- Generally, erosion and deposition sites are local net atmospheric C sinks and sources, respectively, but exceptions exist

Correspondence to:

P. Kumar,
kumar1@illinois.edu

Citation:

Yan, Q., Le, P. V. V., Woo, D. K.,
Hou, T., Filley, T. R., & Kumar, P.
(2019). Three-dimensional modeling
of the coevolution of landscape
and soil organic carbon. *Water
Resources Research*, 55, 1218–1241.
<https://doi.org/10.1029/2018WR023634>

Received 6 JUL 2018

Accepted 21 DEC 2018







Accepted article online 27 DEC 2018

Published online 11 FEB 2019

Corrected 22 APR 2019

This article was corrected on 22 APR
2019. See the end of the full text for
details.

Three-Dimensional Modeling of the Coevolution of Landscape and Soil Organic Carbon

Qina Yan¹ , Phong V. V. Le^{1,2} , Dong K. Woo¹ , Tingyu Hou³ , Timothy Filley³ ,
and Praveen Kumar^{1,4} 
¹Department of Civil and Environmental Engineering, University of Illinois at Urbana-Champaign, Urbana, IL, USA,

²Now at Faculty of Hydrology Meteorology and Oceanography, Vietnam National University, Hanoi, Vietnam,

³Department of Earth, Atmospheric, and Planetary Sciences, Purdue University, West Lafayette, IN, USA, ⁴Department of Atmospheric Sciences, University of Illinois at Urbana-Champaign, Urbana, IL, USA

Abstract Soil organic carbon (SOC) is going through rapid reorganization due to anthropogenic influences. Understanding how biogeochemical transformation and erosion-induced SOC redistribution influence SOC profiles and stocks is critical to our food security and adaptation to climate change. The important roles of erosion and deposition on SOC dynamics have drawn increasing attention in the past decades, but quantifying such dynamics is still challenging. Here we develop a process-based quasi 3-D model that couples surface runoff, soil moisture dynamics, biogeochemical transformation, and landscape evolution. We apply this model to a subcatchment in Iowa to understand how natural forcing and farming practices affect the SOC dynamics in the critical zone. The net soil thickness and SOC stock change rates are -0.336 (mm/yr) and -1.9 (g C/m²/year), respectively. Our model shows that in a fast transport landscape, SOC transport is the dominant control on SOC dynamics compared to biogeochemical transformation. The SOC profiles have “noses” below the surface at depositional sites, which are consistent with cores sampled at the same site. Generally, erosional sites are local net atmospheric carbon sinks and vice versa for depositional sites, but exceptions exist as seen in the simulation results. Furthermore, the mechanical soil mixing arising from tillage enhances SOC stock at erosional sites and reduces it at depositional ones. This study not only helps us understand the evolution of SOC stock and profiles in a watershed but can also serve as an instrument to develop practical means for protecting carbon loss due to human activities.

Plain Language Summary Understanding how soil organic carbon (SOC) content changes in space and time are critical for our food security and adaptation to climate change. It changes through the belowground transformation—decomposition of litter and release of CO₂, and surficial transport—lateral physical redistribution. The balance between the two interactions has been strongly shifted by human activities. Quantifying such interactions has remained challenging. Here we developed a 3-D model, which simulates the movement and burial of SOC and compare the impacts of natural and human activities in the critical zone. We apply this model to a watershed in Iowa. Our results show that the net soil thickness and SOC stock change rates are both decreasing. The fast burial of legacy carbon by modern carbon results in a “nose” profile at depositional sites, which is consistent with soil cores sampled in the watershed. The lateral transport rate can be significantly larger than the transformation rate, but this balance is modified by the mechanical mixing from tillage. Generally, erosional sites are net sinks for atmospheric carbon and depositional sites are net sources. The model can serve as an important tool for protecting soil carbon change caused by both human and natural events.

1. Introduction

Agricultural practices in arable land have drastically accelerated soil erosion and altered soil organic carbon (SOC) dynamics from an undisturbed state (Amundson et al., 2015). Globally, 33–35 Pg/year of sediment flux is mobilized in agricultural land (Borrelli et al., 2017; Quinton et al., 2010; Van Oost et al., 2007), and the associated SOC lateral flux ranges from 0.35 to 0.65 Pg/year (Doetterl et al., 2016; Quinton et al., 2010; Van Oost et al., 2007). Accelerated soil transport not only redistributes surface SOC but influences the biogeochemical transformation belowground. This biogeochemical transformation of organic carbon in soils

is a result of the input from plant residue and the output from metabolic losses as CO_2 , which leads to a net carbon (C) flux between the soil and atmosphere (Harden et al., 1999). The global estimation of erosion-induced net C exchange to atmospheric CO_2 varies widely from 0.06 to 1.2 Pg C/year as C sink (Berhe et al., 2007; Smith et al., 2001; Stallard, 1998; Van Oost et al., 2007) and from 0.1 to 1 Pg C/year as C source (Ito, 2007; Lal, 2004, 2008). Even though focusing on different spatial and temporal scales would result in different conclusions, the relatively high discrepancy among studies is due to the incomplete understanding and accounting of the fate of eroded and buried SOC and the rate of SOC replacement (Doetterl et al., 2016). This work uses modeling approaches to develop insights about decade- to century-scale SOC evolution due to the coupled processes of SOC transformation and soil transport and resultant landscape evolution throughout the soil column at a watershed scale.

In an undisturbed natural system where SOC has evolved over centuries to millennium, the feedback mechanism between biogeochemical transformation and soil and SOC transport is able to maintain a dynamic equilibrium of C cycle (Amundson et al., 2015). Agricultural practices, however, have significantly perturbed the system, and, hence, disturbed this equilibrium (Amundson et al., 2015; Lehmann & Kleber, 2015). In the intensively managed agricultural landscapes in the U.S. Midwest, farming practices such as changing land cover/land use, tilling the surface soil, and installing tile drainage networks belowground have pushed the soil system away from equilibrium conditions toward accelerated soil and SOC erosional loss (Kumar et al., 2018). By analyzing soil samples up to 100 cm deep in central Illinois (sampled in early 1900s, 1957, and early 2000s, respectively), David et al. (2009) found that cultivated fields had SOC typically 30% to 50% less than undisturbed nearby prairie soils. However, it is unclear how the accelerated SOC erosion/deposition and the altered SOC transformation affect the mechanisms and magnitudes of SOC dynamics in an agricultural watershed.

The role of soil transport in SOC biogeochemical transformation has drawn increasing attention since the work done by Stallard (1998). Biogeochemical transformation of SOC can be summarized into two competing processes—SOC accumulation (from plant residues) and decomposition (by soil microbes)—which are two opposing vertical C fluxes of the soil-atmosphere exchange. Some factors control transformation directly such as soil physical properties, soil moisture, and land use/land cover. Soil transport, on the other hand, controls the transformation indirectly by changing the magnitude and turnover rate of SOC. Soil transport mobilizes SOC through erosion, breaks aggregates apart, and in depositional areas buries the already existing layer of SOC. Soil lateral flux redistributes SOC and, hence, changes the SOC stocks and profiles. At erosional sites, the newly exposed subsoil could favor C sequestration and provide local net sinks of atmospheric C because the rate of decomposition is generally slower than accumulation (Doetterl et al., 2016; Quinton et al., 2010; Van Oost et al., 2007). At depositional sites, top soil layers with relatively high SOC content are gradually buried into deeper layers. The burial suppresses SOC turnover rate but increases the total amount of SOC, which would either reduce or enhance SOC decomposition rate. Hence, depositional sites could either serve as local net atmospheric CO_2 sinks or sources (Berhe et al., 2008; Berhe & Torn, 2017; David et al., 2009; Wang et al., 2014; Wiaux et al., 2014; Van Oost et al., 2007; Zieger et al., 2017). Although we acknowledge that emerging conceptual models of SOC dynamics address a realistically grounded perspective (Lehmann & Kleber, 2015), explicitly modeling of these processes has not been achieved. Here we use a process-based model to understand how soil transport, the resultant landscape evolution, and biogeochemical transformation affect the lateral and vertical SOC dynamics under both natural and human influences.

Study of spatial SOC dynamics (i.e., over a watershed) is challenging because the spatial variability across scales ranging from climate, geology, biota, to microtopographic features influence a range of biogeochemical and ecohydrological processes (Le & Kumar, 2017; Thompson et al., 2010; Wolf et al., 2011). Moreover, factors related to the SOC dynamics, including microbes, vegetation, topography, and mineralogy have different temporal scales of evolution (e.g., from days to centuries; Porporato et al., 2003; Quijano et al., 2013; Woo et al., 2014). A comprehensive understanding of the fate of eroded and buried SOC and the rate of SOC replacement from a watershed to regional and global scales through direct observation would be incredibly hard and costly because it would require extensive sampling and complex laboratory experiments. Therefore, a process-based model is an ideal tool to understand how soil transport and resultant landscape evolution and biogeochemical transformation affect the spatial and vertical SOC dynamics under both natural and human influences.

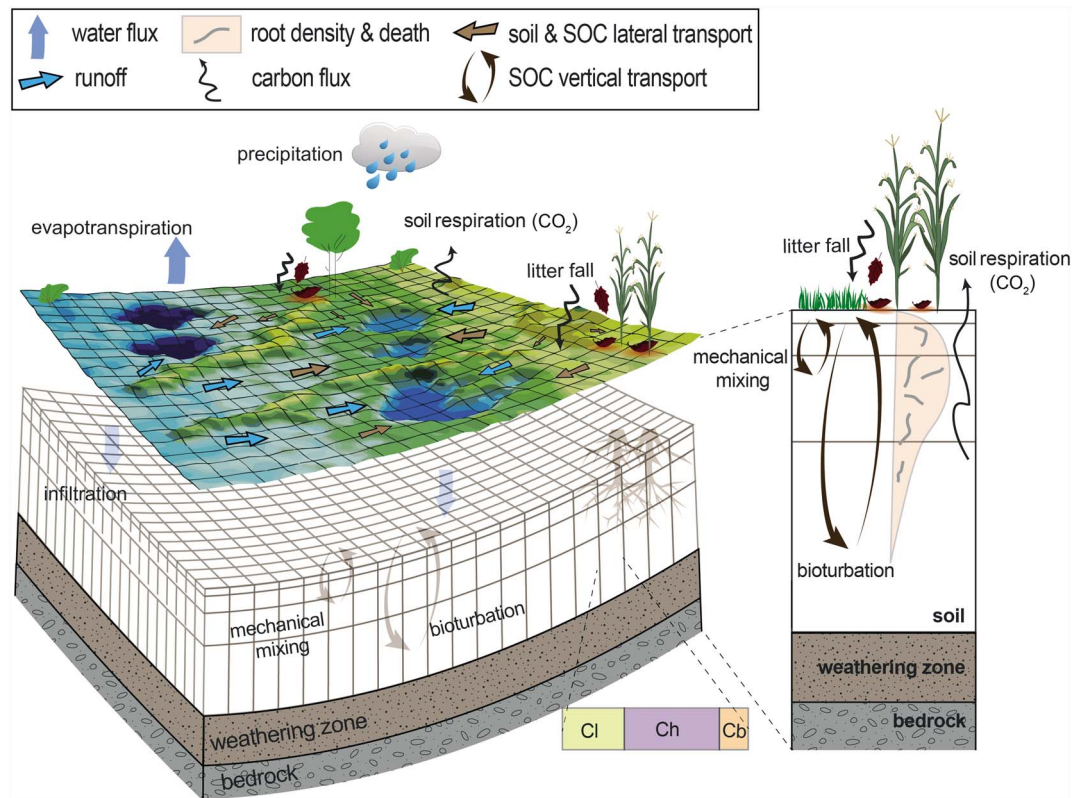


Figure 1. Schematic of the modeling framework that couples biogeochemical transformation related processes of SOC through the soil column with geomorphological transport at the surface. Overland flow and soil moisture are codependent through infiltration and evaporation. SOC turnover is controlled by soil moisture, plant residue input (e.g., leaf litter-fall, dead root, and stover), bioturbation by soil fauna, mechanical soil mixing, and SOC surface transport. Soil transport and resultant landscape evolution are directly controlled by overland flow, wind, and rain splash. The associated SOC transport provides an upper boundary condition for the belowground biogeochemical transformation. Three SOC pools are considered here: fast (C_f), slow (C_h), and microbial biomass (C_b) pools. These three pools interact with each other and exchange C between soil and atmosphere by accumulating SOC from plant residues and releasing CO₂ through decomposition of the metabolic. The computational approach discretizes the surface processes as 2-D matrix and belowground processes using a 1-D array, where the surface processes include overland flow, soil transport, and surface SOC transport and belowground processes include soil moisture and SOC transformation. SOC = soil organic carbon.

Ideally, a model that simulates SOC dynamics at a watershed scale should be capable of capturing both short- and long-term processes with a high temporal and spatial resolution. However limitations exist due to parameterization, insufficient sampling data, lack of full understanding of physical processes, and computational cost. In the past two decades, several models have been developed such as WEPP and CENTURY (Harden et al., 1999; Liu, 2003; Yadav & Malanson, 2009), SPEROS-C (Dlugoš et al., 2012; Wang et al., 2014; Van Oost et al., 2005), and SORCERO (Billings et al., 2010). These models simplify processes either by assigning a constant erosion rate on a single eroding soil profile, using annual or larger time step, which ignore processes within this time window, or assuming an exponentially decreasing SOC profile, which may not always be the case in the field (David et al., 2009; Zieger et al., 2017). Overall, these models do not couple hydrologic, geomorphologic, and biogeochemical processes that fully represent the rate of SOC erosion and deposition and the fate of eroded and buried SOC undergoing transformation. A recent study conducted by Dialynas et al. (2016) used a physically based approach that addresses the heterogeneity at fine spatial scales of SOC erosion and associated soil-atmosphere C fluxes. However, the vertical SOC profiles are estimated by fitting an exponential function, and the decomposition and accumulation rates are prescribed as constants, making them independent of direct influences such as the variability of soil moisture and microbial dynamics.

In this work, we develop a process-based model that couples hydrological, biogeochemical, and geomorphological processes with high spatial (2 m) and temporal (daily) resolution. This model addresses how landscape evolution and biogeochemical transformation affect the spatial distribution of SOC vertical profiles and SOC stocks under anthropogenic influences. In section 2, we introduce the modeling framework and show how different processes are coupled together. Then, in section 3, we describe the study site, a first order subcatchment of the Clear Creek Watershed (CCW) in Iowa and one of the watersheds of the Intensively Managed Landscapes Critical Zone Observatory (IML-CZO). Observed data from soil cores and model parameterization are also included in this section. Then, in section 4, we discuss simulation results and their implications. We compare the SOC vertical profiles between modeling results and observation from soil samples and investigate the roles of erosion and deposition on the local net soil-atmosphere C exchange. We also show the impacts of mechanical soil mixing arising from conventional tillage on SOC dynamics in the subcatchment. Finally, in sections 5 and 6, we provide discussion and conclusion.

2. Model Description

To fully understand the fate of eroded and buried SOC and the rate of SOC replacement, our model, named SCALE (Soil Carbon and Landscape co-Evolution), captures surface SOC transport as a result of soil transport in landscape evolution model, SOC erosion or burial, and the decomposition or gain of SOC throughout the vertical soil column. SCALE incorporates an explicit quasi 3-D framework (Figure 1) to explore the coevolution of landscape and SOC dynamics. This quasi 3-D model couples five major components—(i) overland flow, (ii) soil moisture dynamics, (iii) soil organic matter transformation, (iv) soil transport and resultant landscape evolution, and (v) the associated SOC lateral transport.

Coupling these five components bridges the gap between 2-D surface transport and 1-D belowground biogeochemical transformation in modeling SOC dynamics. The 2-D surface processes include overland flow, soil transport, and organic matter transport, and the 1-D belowground processes include soil moisture dynamics and biogeochemical transformation, which resolves the SOC dynamics along the soil depth by using multiple soil layer structure. Surface and belowground processes are coupled directly through infiltration/evapotranspiration and bioturbation and indirectly via shared variables as described in subsections below. This quasi 3-D model considers spatial and temporal variabilities of water cycle, C cycle, and topography evolution from days to centuries.

In this section, the models of overland flow and soil moisture are briefly reviewed first (Le et al., 2015). SOC transformation is described next, which is based on the work done by Porporato et al. (2003). The soil erosion/deposition and associated SOC transport are then presented. The core of this integrated model is in section 2.6, which provides a detailed description of coupling of biogeochemical transformation with physical transport. Tillage and vertical soil column discretization are discussed after that. The parameters of model inputs are listed in Table 1.

2.1. Overland Flow

Overland flow occurs when the rainfall intensity exceeds the infiltrability of the soil (infiltration excess) or the soil becomes saturated from below (saturation excess). Overland flow controls the belowground soil moisture dynamics (section 2.2) and transports soil from high to low elevation (section 2.4).

Overland flow equations are commonly derived from the Saint-Venant equations, which include the continuity and momentum conservation equations. By combining the two equations with Manning's equation, Lal (1998) derived a 2-D water surface elevation equation in a diffusive form. The diffusion approximation is applicable over a range of temporal resolutions (i.e., from subhourly to daily) and flow conditions, especially low-relief landscapes as in this study:

$$\frac{\partial H}{\partial t} = \frac{\partial}{\partial x} \left(D_h \frac{\partial H}{\partial x} \right) + \frac{\partial}{\partial y} \left(D_h \frac{\partial H}{\partial y} \right) - q_e + I, \quad (1)$$

where H is water surface elevation [L], which equals the sum of surface elevation (η [L]) and water depth (h [L]); t is time [T]; x and y are distance along two perpendicular lateral directions; I is precipitation with interception subtracted [$L T^{-1}$] (section 3.2); q_e is the net exchange flux between surface and subsurface,

Table 1
Parameters of Model Inputs

Parameter	Symbol	Units	Value
Overland flow			
Manning's value for vegetation	n_v	s/m ^{1/3}	0.09 ^a
Manning's value for bare soil	n_b	s/m ^{1/3}	0.025 ^a
Soil moisture			
Saturated water content, or porosity	θ_s	[–]	0.477 ^b
Pore size distribution	n_p	[–]	2.0 ^b
Saturated hydraulic conductivity	K_{sat}	m/day	$4.8 \times 10^{-4(a,b)}$
Residual water content	θ_r	[1/m]	0.08
Specific storage coefficient	S_s	[–]	5×10^{-4}
Field capacity	θ_{fc}	[–]	0.143
Soil surface evaporation rate	E_s	m/day	3.2×10^{-4}
Plant total transpiration rate	T_{max}	m/day	9.1×10^{-4}
Soil organic matter			
Litter (harvest) on the surface for corn and soybean	$I_{\text{litter}}^{sf,h}$	kg C/m ³ /yr	450 and 60 ^c
Litter (harvest) belowground for corn and soybean	$I_{\text{litter}}^{bg,h}$	kg C/m ³ /yr	200 and 130 ^c
Decomposition coefficient for fast/litter pool	k_l	m ³ /day/g C	see foot note ^d
Decomposition coefficient for slow/humus pool	k_h	m ³ /day/g C	see foot note ^d
Death rate of microbial biomass	k_{rd}	1/day	see foot note ^d
Bioturbation diffusivity at the surface	D_{top}	m ² /year	$(4 \times 10^{-4})^e$
Sediment transport			
Soil linear diffusion coefficient in x and y directions	D_y	m ² /year	0.024 ^f and 0.024 ^f
Critical shear stress	τ_c	km/m/s ²	5.6 ^a
Rill erosion coefficient	K_r	s/m	0.005 ^a
Sheet erosion coefficient	K_{qs}	[–]	0.00015 ^a
Sheet erosion coefficient	α	[–]	1.6 ^a
Soil bulk density	ρ_s	kg/m ³	1.34×10^3
Glacial rebound	U	m/year	0.0
Soil weathering rate	P	m/year	0.0
Vegetation			
Time from leaves visible to fall for corn and soybean	σ	day	41 ^b and 26 ⁱ
Specific leaf area for corn and soybean	SLA	m ² /g	$(1.8 \times 10^{-2})^j$ and $(2.2 \times 10^{-2})^k$
C mass percentage of dry leaf for corn and soybean	$C\%$	%	41.27 ^l and 35.20 ^m
Tillage			
Plowing depth	Z_m	m	0.20
Tillage time each year	DOY_{till}	day	105

^aAbaci and Papanicolaou (2009). ^bEstimated using empirical relationship for silt clay loam soil texture (Clapp & Hornberger, 1978). ^cWoo et al. (2014). ^d k_l , k_h , and k_{rd} are solved by assuming the initial SOC profiles are in steady state by assigning $g = 0$ (equation (7)). ^eQuijano et al. (2013). ^fFernandes and Dietrich (1997). ^gKilinc and Richardson (1973). ^hHanway (1966). ⁱHanway and Thompson (1967). ^jDanalatos et al. (1994). ^kScott and Batchelor (1979). ^lLatshaw and Miller (1924). ^mSrivastava et al. (2006).

Table 2
Variables and Initial Values Used in the Case Study

Variables	Symbol	Units	Initial value
Overland flow variables			
Surface water elevation	H	m	Same as DEM
Surface water depth	h	m	0.0
Sediment transport variables			
Land surface elevation	η	m	DEM input
Soil depth of each layer	Z	m	0.05, 0.11, 0.19, 0.29, 0.42, 0.62, 1.0 ^a
Soil moisture variables			
Pressure head	Ψ	m	−2.7, −2.9, −3.1, −3.3, −3.6, −3.9, −4.5 ^a
Soil moisture	θ	[−]	0.46, 0.45, 0.45, 0.45, 0.44, 0.44, 0.43 ^a
Soil organic matter parameters			
Carbon in fast (or litter) pool	C_l	kg C/m ³	6.0, 5.1, 4.2, 3.3, 2.4, 1.5, 0.6 ^{a,b}
Carbon in slow (or humus) pool	C_h	kg C/m ³	37.5, 31.9, 26.3, 20.6, 15.0, 9.3, 3.5 ^{a,b}
Carbon in biomass pool	C_b	kg C/m ³	0.16, 0.13, 0.11, 0.086, 0.062, 0.038, 0.014 ^{a,b}

Note. DEM = digital elevation model.

^aFrom surface to bottom. ^bThe carbon profile of each pool is a function of soil depth, $C_i = C_i^{\text{top}} e^{-2.5Z}$, where C_i^{top} is the soil organic carbon concentration on the surface, and $i \in \{l, h, b\}$.

including infiltration and evaporation [$L T^{-1}$]. The diffusion coefficient D_h [$L^2 T^{-1}$] is expressed as

$$D_h(H, h) = \begin{cases} \frac{h^{5/3}}{n\sqrt{S_h}}, & \text{if } h > h_{\min}, \\ 0, & \text{otherwise,} \end{cases} \quad (2)$$

where n is Manning's coefficient [$TL^{-1/3}$]. Manning's coefficient may vary in time and space. In this study, we choose two Manning's coefficients for vegetation (0.025 s/m^{1/3}) and bare soil (0.09 s/m^{1/3}) corresponding to either positive or zero values of the leaf area index (section 3.2), respectively. To build up the complexity of the model, one can consider Manning's coefficient in relationship with dynamic biomass (Yetemen et al., 2015) as needed. S_h is the slope of water surface [−]:

$$S_h = \sqrt{(\partial H / \partial x)^2 + (\partial H / \partial y)^2}. \quad (3)$$

The initial input is the water depth (h) on each surface grid for the entire simulation domain. It can be zero or a reasonable water ponding depth either spatially uniform or nonuniform. The boundary conditions of water depth (h) in the numerical solution can be either Dirichlet condition (specific water depth) or Neumann condition (specific flow flux). In the case study (section 4), we choose a zero water depth as the initial conditions and free outflow (Neumann condition) as the boundary conditions.

2.2. Soil Moisture Dynamics

Soil moisture interacts with surface water flow and plays a critical role in the SOC biogeochemical transformation because it controls microbial activity that decomposes SOC (Porporato et al., 2003; Wieder et al., 2013). Our initial soil column is 1 m deep and has seven layers (see the thickness of each layer in Table 2), and soil moisture dynamics are simulated using Richards' equation (Richards, 1931) in a mixed form (Celia et al., 1990; Clement et al., 1994):

$$S_s \frac{\theta}{\varphi} \frac{\partial \Psi}{\partial t} + \frac{\partial \theta}{\partial t} = \nabla \cdot K(\theta) [\nabla \Psi + \vec{k}] + q'_e, \quad (4)$$

in which θ is soil moisture [−]; Ψ is subsurface pressure head [L]; S_s is the specific storage coefficient [L^{-1}]; φ is porosity [−]; K is unsaturated hydraulic conductivity [$L T^{-1}$]; \vec{k} is the unit-upward vector; q'_e is the exchange flux between surface and subsurface [T^{-1}], which equals q_e divided by the thickness of the first soil layer.

The relationship between soil moisture, pressure head, and unsaturated hydraulic conductivity is based on a closed-form model by Van Genuchten (1980):

$$K(\theta) = K_{\text{sat}} \Theta^{1/2} \left[1 - (1 - \Theta^{n_p/(n_p-1)})^{1-1/n_p} \right]^2, \quad (5)$$

where n_p is the pore size distribution [–], K_{sat} is the saturated hydraulic conductivity [LT^{-1}], and Θ is the relative saturation [–] that can be derived from the soil-water retention curve (Van Genuchten, 1980):

$$\Theta = \frac{\theta - \theta_r}{\theta_s - \theta_r} = \left[\frac{1}{1 + (\alpha_a \Psi)^{n_p}} \right]^{1-1/n_p}, \quad (6)$$

where θ_r is the residual water content [–], θ_s is the saturated water content [–], α_a is a parameter controlled by the inverse of the air entry suction [L^{-1}]. The retention curve, based on soil structure and properties, could be affected by outside disturbance such as tillage. Here we assume these soil properties are invariant over time, and there is no change in the soil-water retention curve due to disturbance.

The initial input is the subsurface pressure head (Ψ) throughout a soil column for the entire domain. This initial value only has a very short-time (varying from days to weeks) impact on the results because rainfall intensity, the external forcing, has a much stronger influence on the soil moisture. In our simulations, we assign a linearly decreasing negative pressure head as the initial value. The top boundary condition uses a switching procedure of Dirichlet condition (specified head) and Neumann condition (specified flux). It depends on the soil moisture (or pressure head), the ponded water depth, and infiltration capacity of that grid. Specifically, a Dirichlet condition applies if the surface grid reaches a surface ponding condition, soil moisture deficit, or a soil-limited condition of infiltration/exfiltration (Camporese et al., 2010, 2014; Le et al., 2015; Paniconi & Wood, 1993; Sulis et al., 2010); otherwise, a Neumann condition applies, and the infiltration or exfiltration rate equals the rainfall (after subtracting interception) or potential evaporation rate. The bottom boundary conditions are free outflow that the water flux equals the value of unsaturated hydraulic conductivity.

2.3. SOC Transformation

In an undisturbed quasi-equilibrium system, the loss of SOC as CO_2 balances with the input of SOC from plant residues over a long run. In the short-time scale (e.g., seasonal to annual), however, the fluctuations of SOC content are sensitive to hydrologic variability (e.g., soil moisture) and other input sources (e.g., seasonal plant residues). Following the work of Porporato et al. (2003), three pools are considered in the SOC dynamics—fast (or litter, C_l), slow (or humus, C_h), and microbial biomass (C_b) pools. Specifically, the plant residues (including dead leaves, stems, crop stover, and root decay) are considered as external input into the system (section 3.2), and they join the fast pool directly. In this pool, soil microbes metabolize plant residues involving enzymatic oxidation, releasing CO_2 (soil respiration), and generating humus that contributes to the slow pool. The death of soil microbes, as a portion of microbial biomass, also feeds into the fast pool. In the slow pool, the less complex compounds, or less resistant substance, are continuously decomposed by microbes; while the more complex compounds form the humic substance, or resistant humus. In the microbial biomass pool, an approximately 70% of microbial substrate contributes to CO_2 and the rest of it contributes to the microbial biomass (Hopkins et al., 2014). The equations describing the transformation rate of fast, slow, and microbial biomass are given as (Porporato et al., 2003)

$$\begin{aligned} \mathbf{g} &= [\mathbf{g}_l, \mathbf{g}_h, \mathbf{g}_b]^T \\ &= \begin{bmatrix} I_{\text{litter}} + k_{rd}C_b - K_l C_l \\ r_h K_l C_l - K_h C_h \\ (1 - r_r - r_h)K_l C_l + (1 - r_r)K_h C_h - k_{rd}C_b \end{bmatrix}, \end{aligned} \quad (7)$$

where \mathbf{g} is the rate of SOC concentration change in each C pool [$ML^{-3} T^{-1}$]; C_l , C_h , and C_b are the SOC concentration in the fast, slow, and microbial biomass pool, respectively [ML^{-3}]; I_{litter} is the litter input from both aboveground and belowground through litter-fall and root-litter, respectively [$ML^{-2} T^{-1}$] (section 3.2); k_{rd} is the death rate of microbes [T^{-1}]; r_h is referred to as *isohumic* coefficient (Wild, 1988), which is the fraction of decomposing litter that undergoes humification and ranges from 0.15 to 0.35 [–] (Brady & Weil, 1996; O'dorico et al., 2003; Porporato et al., 2003); r_r defines the fraction of decomposed organic C to

CO_2 [–] ($0 \leq r_r \leq 1 - r_h$); K_l and K_h are rate of C decomposition in fast and slow pools, respectively [T^{-1}]. They are regulated by soil moisture and C/N ratio as shown below (Porporato et al., 2003):

$$K_l = \varphi f_d(\theta) k_l C_b, \quad (8)$$

$$K_h = \varphi f_d(\theta) k_h C_b, \quad (9)$$

where k_l and k_h represent the rate of decomposition as a simplified term that encompasses different organic components in the litter and humus pools, respectively [$L^3 T^{-1} M^{-1}$]; φ is a ratio that is from the reduction of the decomposition rate if the immobilization (controlled by nitrogen content) fails to meet the nitrogen demand by the microbes [–]; $\varphi \approx 1$ in agricultural fields where nitrogen supply is usually sufficient from fertilizers; $f_d(\theta)$ [–] represents the soil moisture effects on decomposition (Porporato et al., 2003). The optimistic soil moisture condition is the field capacity, which provide the highest $f_d(\theta)$ (Porporato et al., 2003). Very dry or wet conditions will result in a smaller $f_d(\theta)$ and hence reduce the decomposition rate. The relationship between relative soil moisture (θ) and the index $f_d(\theta)$ is shown below (Porporato et al., 2003):

$$f_d(\theta) = \begin{cases} \frac{\theta}{\theta_{fc}}, & \text{if } \theta \leq \theta_{fc}, \\ \frac{\theta_{fc}}{\theta}, & \text{otherwise,} \end{cases} \quad (10)$$

where θ_{fc} is field capacity [–]. Meanwhile, K_l and K_h are also controlled by soil temperature. The relationship of decomposition rate as a function of soil temperature is not addressed in this study but can be added within this framework as needed.

This module is a composite of first-order ordinary differential equations in time, which requires initial conditions and no boundary conditions. The initial values are the SOC concentration profile at each spatial grid. In this study, we use an exponentially decreasing profile along depth as an initial condition, which can be assumed as representing an undisturbed soil condition in the beginning. The same profile is applied to every horizontal grid box.

2.4. Overland Sediment Transport, Landscape Evolution, and Soil Thickness Change

The mechanisms of soil transport and the resultant landscape evolution can be categorized into two groups: overland flow-driven transport and diffusion-driven transport from other disturbances (e.g., wind, animal, and raindrop splash). The 2-D mass conservation equation follows Exner equation:

$$\frac{\partial \eta}{\partial t} = U - \nabla \cdot q_d - \nabla \cdot q_s, \quad (11)$$

where η is soil surface elevation [L], U is the rate of tectonic uplift or glacial rebound [LT^{-1}], q_d is the volume flux of sediment per unit width by hillslope diffusion [$L^2 T^{-1}$], and q_s is the volume flux of sediment per unit width by overland flow [$L^2 T^{-1}$].

The hillslope diffusion process ($\nabla \cdot q_d$) is a slope-dependent downslope movement. It is a combination of wind erosion, animal disturbance, soil creep, raindrop splash, and biogenic transport. The 2-D equation of q_d is expressed as a linear relationship with slope (Culling, 1960; Furbish & Fagherazzi, 2001):

$$q_d = -D_x \frac{\partial \eta}{\partial x} - D_y \frac{\partial \eta}{\partial y}, \quad (12)$$

where D_x and D_y are the soil diffusion coefficient in x and y directions, respectively [$L^2 T^{-1}$]. The values for the diffusion coefficients are obtained from field study estimation (Table 1). Here we choose the linear form of hillslope diffusion because the study site has a relatively low local gradient. In a relatively steep area, the nonlinear hillslope diffusion form could be adopted (Perron, 2011).

Overland flow provides the shear stress to mobilize the surface soil. Once it exceeds the critical shear stress (the minimum stress for incipient motion of soil particles), soil particles are transported downstream causing sheet and rill erosion. The transport rate is controlled by stream power, which is a function of overland flow rate, slope, and critical shear stress of soil. If soil erosion rate is directly controlled by stream power, landscape evolution model is detachment limited; when it is directly controlled by the divergence of stream power, it is transport limited (Pelletier, 2011). The two conditions coexist in most landscapes. Hence, we

choose a combined form that the elevation change is due to the divergence of stream power but limited by the detachment capacity (Yetemen et al., 2015):

$$\nabla \cdot q_s = \min \left(D_c, \frac{q_{s,\text{out}} - \sum q_{s,\text{in}}}{d_s} \right), \quad (13)$$

where D_c is the detachment capacity, which is the upper limit of local erosion rate [L/S]; d_s is the width of a grid on the 2-D surface numerical domain [L]; $q_{s,\text{out}}$ is the sediment flux out of a cell; $\sum q_{s,\text{in}}$ is the total sediment flux into a cell assumed at sediment transport capacity.

Both D_c and q_s have power law relationships with along-channel slope and the flow rate (or depth; Dietrich et al., 2003; Howard & Kerby, 1893; Pelletier, 2011). Such relationships can be expressed in different forms (Prosser & Rustomji, 2000). Here we adopt the expression of D_c used in agricultural fields (Foster et al., 1995; Papanicolaou et al., 2015) and q_s in a general form of sediment transport capacity (Julien & Simons, 1985):

$$D_c = \frac{K_r}{\rho_s} (\tau - \tau_c), \quad (14)$$

$$q_s = K_{qs} (\tau - \tau_c)^\alpha, \quad (15)$$

where K_r is the soil erodibility factor [TL^{-1}]; ρ_s is soil bulk density [ML^{-3}]; τ is the flow shear stress [$ML^{-1} T^{-2}$], given as $\tau = \rho_w g h S$ (where ρ_w is fluid density [ML^{-3}]; g is the gravity acceleration [$L T^{-2}$]; S is the slope along flow direction [–]; and h is the surface water depth [L] solved in section 2.1); τ_c is the critical shear stress [$ML^{-1} T^{-2}$]; K_{qs} is sediment transport coefficient [$T^{2\alpha-1} L^{1+\alpha} M^{-\alpha}$]; the values of K_r , K_{qs} , and τ_c are obtained from in situ experiments within the same watershed Abaci & Papanicolaou, 2009; Table 1).

The soil thickness serves as the control volume in SOC dynamics. The rate of soil thickness (Z) change is controlled by landscape evolution on the surface and soil weathering rate belowground. The mass conservation equation for total soil thickness is

$$\frac{\partial Z}{\partial t} = \frac{\partial \eta}{\partial t} + P, \quad (16)$$

where Z is the soil thickness [L] and P is the soil weathering rate [LT^{-1}]. In an agricultural fields, however, the surface soil erosion rate is 1 to 4 orders of magnitude higher than soil weathering rate (Montgomery, 2007). Therefore, P is assumed to be 0 in our simulation. The soil formation processes (Finke & Hutson, 2008; Temme & Vanwalleghe, 2016; Vanwalleghe et al., 2013) can be potentially added into this model to build up further complexity if pedogenesis is of interest.

The initial surface elevation is obtained from LiDAR data (section 3). The boundary conditions are periodic boundary condition that the output flux is same as the input one at the two opposite sides. At the outlets, sediment fluxes are assumed to be free outflow.

2.5. SOC Lateral Transport

The rate of change of SOC on the surface driven by soil transport is the divergence of SOC transport flux per unite width, $\nabla \cdot \mathbf{q}_C$, which has a linear relationship with soil transport flux:

$$\nabla \cdot \mathbf{q}_C = \nabla \cdot (k_{\text{soc}} \mathbf{C}_1 q_d) + \nabla \cdot (k_{\text{soc}} \mathbf{C}_1 q_s), \quad (17)$$

where $\mathbf{C} = [C_l, C_h, C_b]^T$ and the subscript 1 denotes the surface soil layer; q_d and q_s are soil transport flux of diffusion and overland flow; k_{soc} is an enrichment ratio, which represents a preferential transport (mobilization and deposition) of SOC. Since the preferential transport of SOC is affected by the size fractions of aggregates, soil texture, rainfall event, and SOC content, the enrichment ratio has a spatial heterogeneity (Foster et al., 1995; Papanicolaou et al., 2015). However, based on in situ experiment conducted in the CCW (Papanicolaou et al., 2015), k_{soc} is close to 1 at a monthly time scale. In our model, we simulate a 100-year dynamics; hence, we assume $k_{\text{soc}} = 1$. However, the complexity of the model can be built up by giving spatially and temporally varying k_{soc} as needed. The SOC fluxes for diffusion and overland flow sediment transport are

$$\nabla \cdot (k_{\text{soc}} \mathbf{C}_1 q_d) = -\frac{\partial}{\partial x} \left(k_{\text{soc}} \mathbf{C}_1 D_x \frac{\partial \eta}{\partial x} \right) - \frac{\partial}{\partial y} \left(k_{\text{soc}} \mathbf{C}_1 D_y \frac{\partial \eta}{\partial y} \right), \quad (18)$$

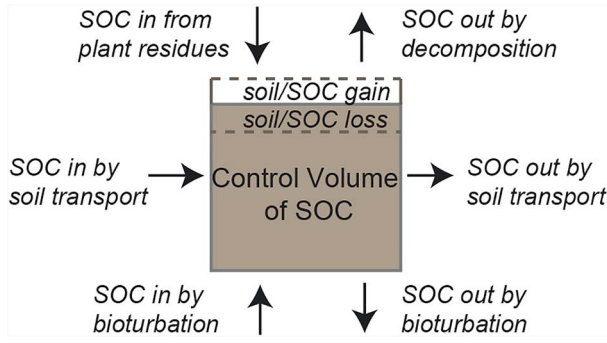


Figure 2. Illustration of the SOC fluxes in a 1-D control volume. Biogeochemical transformation—decomposition and gain from plant residues provides a vertical flux of carbon exchange between soil and the atmosphere. Soil erosion and deposition provides the lateral flux of SOC. The bioturbation, approximated as diffusive mixing of SOC, also provides a vertical flux within the soil column. The height of the control volume keeps changing because of the total soil thickness increases or decreases caused by surface soil erosion/deposition. SOC = soil organic carbon.

$$\nabla \cdot (k_{\text{SOC}} \mathbf{C}_1 \mathbf{q}_s) = \begin{cases} k_{\text{SOC}} \mathbf{C}_1 D_c, & \text{if } D_c < \frac{q_{s,\text{out}} - \sum q_{s,\text{in}}}{d_s}, \\ \frac{k_{\text{SOC}} \mathbf{C}_{1,\text{out}} q_{s,\text{out}} - \sum (k_{\text{SOC}} \mathbf{C}_{1,\text{in}} q_{s,\text{in}})}{d_s}, & \text{otherwise.} \end{cases} \quad (19)$$

2.6. Coupling SOC Transport and Transformation

In a control volume, the time rate of change of SOC in a soil layer is a sum of SOC decomposition as an internal “destruction,” SOC gain from plant (leaf and root) residues as an internal “production,” SOC lateral flux by soil transport, and the vertical flux of bioturbation by soil fauna (Figure 2). The simulated variables as well as the initial values are summarized in Table 2. This control volume has a changing domain space vertically at each time step due to erosion and deposition, which is discussed in the next subsection.

Combining the biogeochemical transformation, soil erosion/deposition (and resultant landscape evolution), and bioturbation by soil fauna, the SOC mass conservation in a soil column is summarized below:

$$\frac{\partial}{\partial t} \int_0^Z \mathbf{C} dz = \int_0^Z \mathbf{g} dz - \nabla \cdot \mathbf{q}_C + \int_0^Z \nabla \cdot [D(z) \nabla \mathbf{C}] dz, \quad (20)$$

where \mathbf{C} is the SOC concentration [ML^{-3}], $\mathbf{C} = [C_l, C_h, C_b]^T$ represents the fast (or litter), slow (or humus), and microbial biomass pool, respectively; \mathbf{g} is the rate of the biogeochemical transformation process; $\nabla \cdot \mathbf{q}_C$ is the surface SOC flux by diffusion erosion and sheet erosion; and the last term of this equation, $D(z) \frac{\partial^2 \mathbf{C}}{\partial z^2}$, is the vertical bioturbation by soil fauna modeled as a diffusion process, where $D(z)$ is the bioturbation diffusivity, parameterized as $D(z) = D_{\text{top}} e^{-0.1z}$ (Quijano et al., 2013).

2.7. Tillage and Mechanical Mixing

Tilling is used for preparing a seedbed for planting and generally includes conservation tillage (<5-cm depth) and conventional tillage (12.5- to 25-cm depth; Hendrix et al., 1988; Li et al., 1994; Potter et al., 2006). We categorize the direct impacts of tillage on soil and SOC into two groups—loosing soil structure and mixing the SOC vertical concentration within the tillage depth. So far, we have considered the accelerated soil erosion as one aspect of loosening soil structure (section 2.4). In this subsection, we address the impacts of mechanical

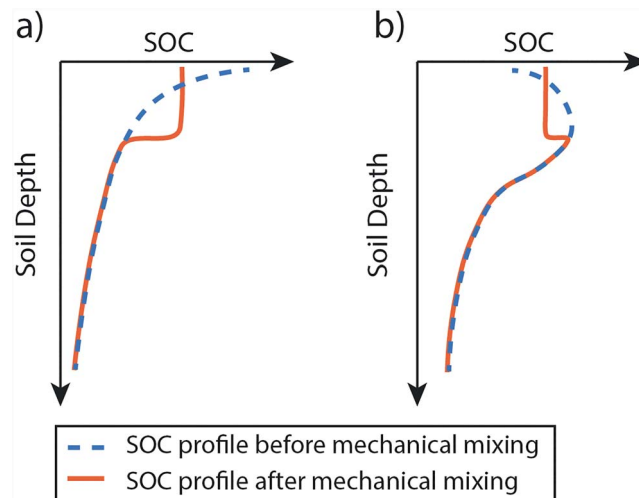


Figure 3. Illustration of the impact of mechanical mixing on different SOC profiles—(a) exponentially decreasing and (b) a “nose” (or “bump”) below the surface. SOC = soil organic carbon.

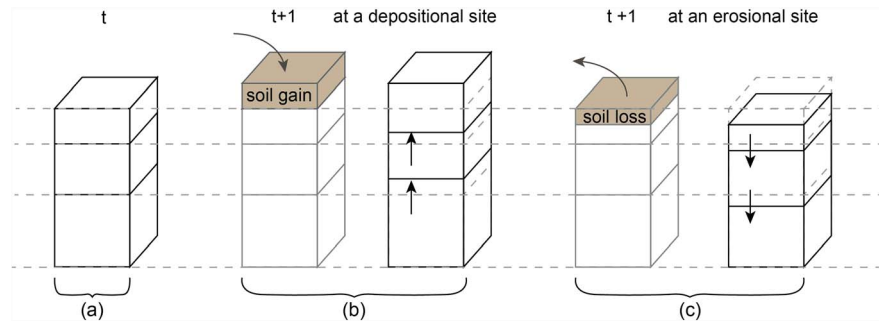


Figure 4. Illustration of the vertical discretization of a soil layer resulting from depositional gain or erosional loss. The example uses three layers to show how layer thickness is adjusted. Initially, (a) the soil thickness of each layer is nonuniform. The ratio of grid size of each layer follows an exponential increase with depth. At the next time step, if a grid gains (b) or loses (c) soil, the total soil thickness changes, and the new grid size of each layer is recomputed based on the same ratio as the earlier one. The soil organic carbon content is appropriately interpolated to maintain mass conservation.

soil mixing. The mechanical soil mixing, once per year before seeding, resets the SOC profile to a vertically uniform value within the top tillage depth (e.g., 20 cm) as shown in Figure 3.

Right after mechanical mixing, the SOC concentration within the mechanical mixing depth should be updated so that the SOC mass is conserved:

$$\mathbf{C}^m = \frac{\int_0^{Z_m} \mathbf{C} dz}{Z_m}, \quad (21)$$

where \mathbf{C} and \mathbf{C}^m are the SOC concentration before and after the mixing mechanical mixing within the mechanical mixing depth, Z_m (e.g., 20 cm), respectively.

2.8. One-Dimensional Soil Column Discretization

The 3-D model domain is discretized into grid boxes, both horizontally (Δx , Δy) and vertically (Δz) for the solution of the governing equations described above. The lateral SOC transport aboveground and the bioturbation process belowground are two independent processes. Hence, equation (20) can be expressed for aboveground and belowground processes, separately:

$$\begin{aligned} \frac{\partial \mathbf{C}_1}{\partial t} &= \mathbf{g}_1 - \nabla \cdot \mathbf{q}_C, \\ \frac{\partial \mathbf{C}_n}{\partial t} &= \mathbf{g}_n + \nabla \cdot [D(z) \nabla \mathbf{C}], \end{aligned} \quad (22)$$

where subscripts 1 and n denote the surface soil layer and the n th layer below surface, respectively.

The horizontal domain and grid boxes (Figure 1) do not change in time. However, the vertical domain, that is, total soil depth, are updated every time step because it keeps changing due to erosion and deposition. In this model, we maintain a fixed number of soil layers but with a dynamic soil layer thickness to represent SOC profiles and obtain numerical stability. For evolution over thousand years, a dynamic layer number would be needed (Temme & Vanwalleghe, 2016). The vertical grid size (e.g., Δz_n , ($n = 1, \dots, n_z$), where n_z is the total number of soil layers) is therefore updated at each time step as a result of changes from erosion or deposition.

Figure 4 illustrates three soil layers as an example for how we deal with a changing soil thickness. The soil layer grid size (Δz_n) is not uniformly discretized but based on a ratio that follows an exponential increase with soil depth: Δz_n is smaller near the surface than in the deeper layers. This is because the SOC concentrations near the upper layers in general are higher and more dynamic than the deeper layers. Once the total soil thickness is updated, the new grid size (Δz_n) is adjusted based on the same ratio. The corresponding SOC concentration in each vertical layer is also adjusted based on a linear interpolation that conserves SOC mass. The equations below describe how to adjust Δz_n and \mathbf{C} at each time step:

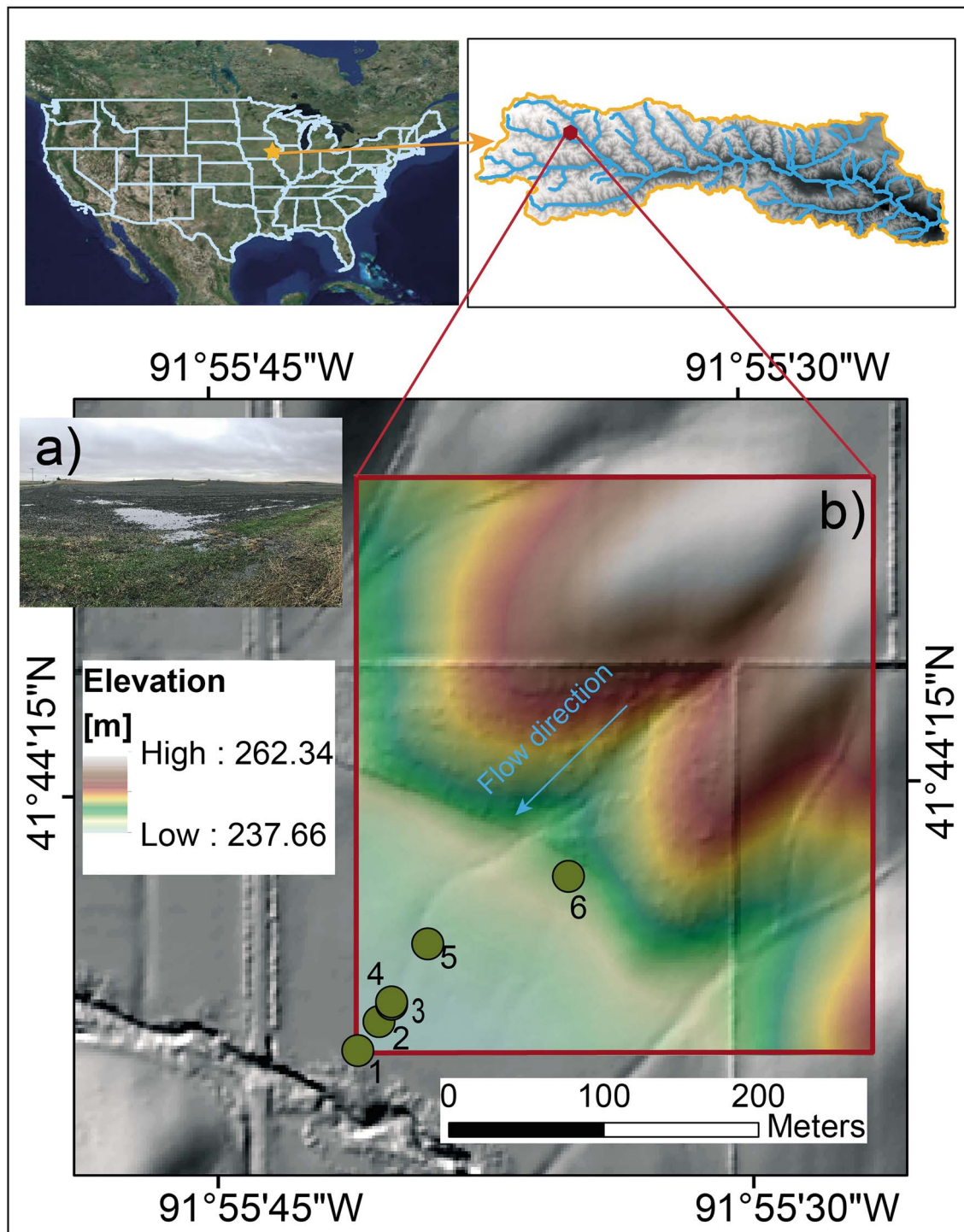


Figure 5. Map of the study site (a subcatchment) in Clear Creek Watershed in Iowa, USA. (a) An overview of the field site (taken on 4 Nov 2018). (b) LiDAR digital elevation model (2-m resolution) of the study site. The six sampling points from which soil cores are drawn to obtain the vertical digital elevation model profiles (see Figure 6) are labeled on the map (i.e., Cores 3 and 4 are very close to each other). Note that the straight lines with a higher local relief are grass strips that serve as boundaries between farmlands.

$$\sum_{n=1}^{n_z} \Delta z_n^{t+1} = \sum_{n=1}^{n_z} \Delta z_n^t + \Delta Z, \quad (23)$$

$$\sum_{n=1}^{n_z} \mathbf{C}_n^{t+1} \Delta z_n^{t+1} = \sum_{n=1}^{n_z} \mathbf{C}_n^{tp} \Delta z_n^t, \quad (24)$$

where n_z is the total number of soil layers, n represents the layer numbers (1 is the surface layer and n_z is the bottom), t represents the values before adjusting soil layer thickness, $(t + 1)$ represents the values after adjusting soil layer thickness, tp represents the \mathbf{C} solved from equation (22) but before adjusting/interpolating to the updated soil layer thickness, and ΔZ represents the soil thickness change (gain or loss) on the surface. When mechanical mixing happens at a certain time step, the SOC concentration, \mathbf{C} , should be further adjusted as

$$\mathbf{C}_n = \frac{\sum_{n=1}^{n_m} \mathbf{C}_n \Delta z_n}{\sum_{n=1}^{n_m} \Delta z_n}, \quad (25)$$

where n_m is the number of layers that fall within the mechanical mixing depth.

In the following sections, we apply our process-based quasi 3-D model for a subcatchment in the agricultural U.S. Midwest. We explain the study site, field samples, and model inputs first and then discuss the simulation results with validation.

3. Study Site, Field Samples, and Data Input

Our study site is a subcatchment of the CCW in east-central Iowa (Figure 5). This subcatchment covers about 0.12 km² in the headwater area. The CCW is part of IML-CZO. CCW was glaciated multiple times by continental advances of the Laurentide Ice Sheet during the Early to Middle Pleistocene (130,000 to 2,580,000 years ago Fan & Hou, 2016). After the retreat of the last glaciation, prairie wetlands were formed and had been undisturbed until the European Settlement in the early 1800s. Agricultural practices has started since then but expanded extensively after the 1900s (Kumar et al., 2018). The erosion rate accelerated significantly with the expansion (Papanicolaou et al., 2015).

3.1. Field Samples

Six soil cores were collected to a maximum depth of 1.2 m in the subcatchment along a transect (Figures 6a and 6b) in 2014. Cores were extracted using a truck-mounted impact corer, described for structural and edaphic properties, then sectioned at approximately 4-cm intervals. Air dried samples of each section were lightly crushed before milling to a fine powder for analysis. Soils were analyzed for SOC content using a Sercon (Crewe, UK) GLS elemental analyzer. The values of SOC content were normalized to weight of soil (Figures 6c1–6c6).

The vertical profiles of SOC, from the laboratory analysis, show a trend from upland to lowland sites, and none of six profiles has exponentially decreasing SOC concentration along the soil depth. A subsurface SOC concentration maximum (bump or nose) is observed in Cores 1–5, and its location becomes deeper as we move toward the lower lying areas laterally. The formation of the nose is hypothesized as arising from the burial of preagricultural SOC, due to accelerated redistribution of upslope eroded material. Even though the six sample cores are close to the Clear Creek, the main sediment deposition source is assessed to come from upland not flood deposition. The influence of sediment deposition from flood can be excluded because the six sampling cores are in a terrace zone (Yan et al., 2017), and all of them are outside of the flood area from the Federal Emergency Management Agency flood map (<http://msc.fema.gov/portal>).

By realigning the SOC profiles, such that the nose overlap with each other (Figure 6d), the parts below the nose are close to an exponentially decreasing curve. This supports our hypothesis that before fast soil erosion happened due to agriculture, the SOC dynamics were probably in balance as an undisturbed natural system. Thereafter, accelerated soil erosion and deposition due to agricultural practices altered the vertical profiles, and since then, plays a dominant role in controlling present day SOC vertical profiles and stocks in the agricultural land.

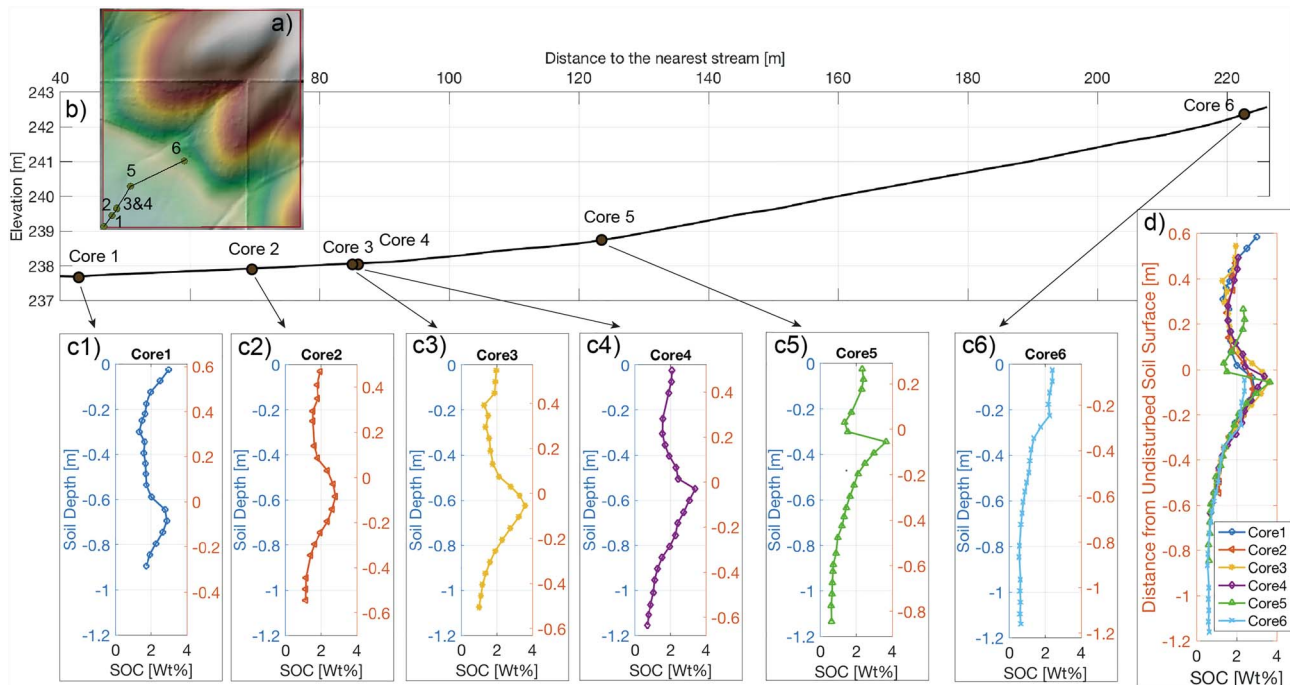


Figure 6. Illustration of the sampled vertical SOC profiles from the six sampling cores. (a) The topography map with six sampling sites. (b) Elevation transect associated with the six cores. (c1–c6) SOC concentration profiles. The y axis on the left is the local soil depth. The y axis on the right is realigned soil depth assuming that the “nose” area corresponds to the preagriculture (or “undisturbed”) soil surface before a fast erosion/deposition took place. (d) Overlapping plots of the six profiles based on the realigned soil depth, and the profiles below the nose follow exponentially declining, which reflects the preagriculture profile. The nose are hypothesized as arising after a fast erosion/deposition took place. SOC = soil organic carbon.

3.2. Input Data

The major model inputs include elevation, soil properties, weather forcing, crop cover, and plant residues. The elevation input is 2-m LiDAR DEM (data source: <http://www.gis.iastate.edu/gisf/projects/acpf/>). Other parameters are summarized in Table 1. The soil properties include soil texture, porosity, field capacity, soil bulk density, and saturated hydraulic conductivity. These values are obtained from soil survey by U.S. Department of Agriculture (USDA; data source: <https://websoilsurvey.sc.egov.usda.gov/>; Table 1). The soil texture (silty clay loam: clay 29%, silt 68%, and sand 3%) and saturated hydraulic conductivity (K_{sat}) are laterally uniform in this subcatchment.

To explore the long-term coupled evolution of SOC and landscape, we target a 100-year simulation with a daily time step. The meteorological data are obtained from a weather station (41°42′36″N, 91°28′40″W) adjacent to Iowa City with 10-year record (2006–2015). These data are used to train a Weather Generator (Ivanov et al., 2007) to generate another 90 years of stochastic meteorological data (Figure 7a).

To estimate the crop residues and overland flow resistance (Manning's coefficient), we generate the daily green leaf area index (gLAI) from the Landsat (7 TEM+). The crop cover is a corn-soybean rotation in alternate years obtained from USDA, so we aim to use a fixed annual pattern, 1 year for corn and the next year for soybean, of gLAI for the entire 100-year simulation. The annual gLAI is based on a 5-year satellite data (January 2013 to December 2017). Specifically, we convert the digital data from radiance to the normalized difference vegetation index (NDVI). We generate the 5-year time sequence of spatial mean values of NDVI for the each type of crop (corn and soybean). Next, we use empirical relationships to calculate gLAI from NDVI for both corn and soybeans (Nguy-Robertson et al., 2012). Finally, we obtain an interannual gLAI by averaging the 5-year data (Figure 7b).

With the gLAI, we can estimate the rate of aboveground litter-fall (L_f) during growing season. The rate of gLAI change equals the rate of growing new leaves (Nl) minus L_f (equation (26); Quijano et al., 2013). Also, L_f is assumed to be equal to Nl with a time lag, which is the time period for a leaf to stay on the plant (Quijano

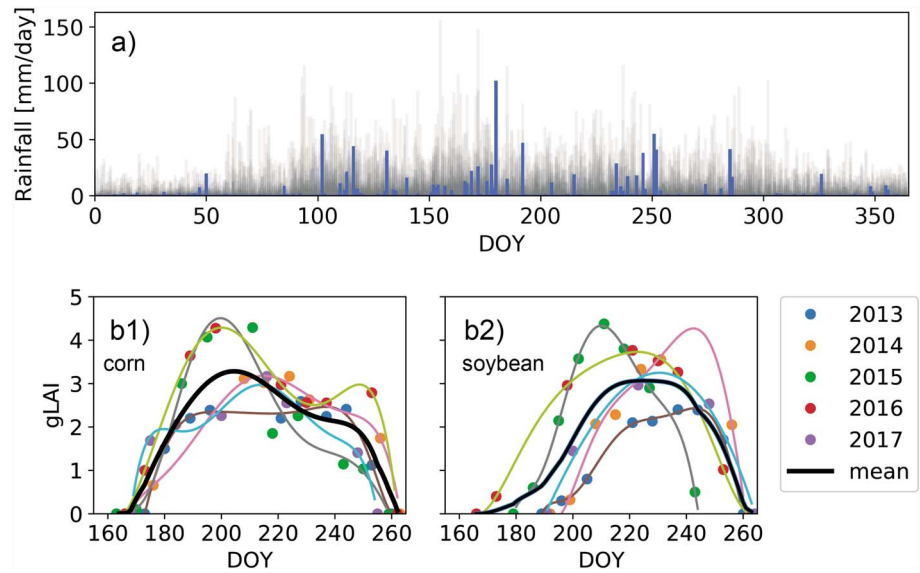


Figure 7. Rainfall and LAI input. (a) Simulated daily rainfall data of 100 years that overlap in an annual frame. The highlighted bars in blue illustrates the observed rainfall in 2014. The rainfall data are collected from a weather station ($N41^{\circ}42'36''$, $W91^{\circ}28'40''$) adjacent to Iowa City with 10-year record (2006–2015), and the additional 90-year data are simulated using a Weather Generator (Ivanov et al., 2007). (b) Green LAIs (gLAI) are processed from Landsat satellite bands for 5 years (2013–2017). The value at each collection day is spatially averaged for the same crop type (corn [b1] or soybean [b2]). The black line is the mean for the 5-year record, which is then used through the simulation period for corn-soybean rotation in alternate years. LAI = leaf area index; DOY = day of year.

et al., 2013):

$$\begin{aligned} Nl(t) &= \frac{d(gLAI(t))}{dt} + Lf(t), \\ Lf(t) &= Nl(t - \sigma), \end{aligned} \quad (26)$$

where Nl is the rate of new leaf production as a fraction of gLAI [$L^2 L^{-2} T^{-1}$], Lf is the rate of litter-fall as a fraction of gLAI [$L^2 L^{-2} T^{-1}$], and σ is the number of days from a leaf being visible till falling [T]. Next, we convert the unit of Lf from leaf area per unit area per unit time ($[L^2 L^{-2} T^{-1}]$) to the C mass per unit area per unit time ($[ML^{-2} T^{-1}]$):

$$I_{litter}^{sf,g} = \frac{L_f}{SLA} * C\%, \quad (27)$$

where $I_{litter}^{sf,g}$ is the surface litter input during the growing season [$ML^{-2}T^{-1}$], SLA is the specific leaf area (defined as leaf area per mass of a drying leaf) [L^2M^{-1}], $C\%$ is the C mass percentage of the total weight in a dry leaf [MM^{-1}] (Danalatos et al., 1994; Latshaw & Miller, 1924; Scott & Batchelor, 1979; Srivastava et al., 2006; see values in Table 1). The total inputs of crop residues include both aboveground and belowground. Also, the growing season and harvest are considered separately as expressed below:

$$I_{litter} = I_{litter}^{sf,g} + I_{litter}^{bg,g} + I_{litter}^{sf,h} + I_{litter}^{bg,h} \quad (28)$$

The belowground residue (also known as root decay) during growing season ($I_{litter}^{bg,g}$) is estimated by multiplying a constant ratio of the aboveground residue input. The ratio is 21% and 35% for corn and soybean, respectively (Quijano et al., 2013; Woo et al., 2014). The vertical distribution of belowground residue is based on the root density fraction for corn and soybean (Amenu & Kumar, 2008). Right after the harvest, tremendous amount of crop residues from stover and dead roots is added to both aboveground and belowground input ($I_{litter}^{sf,g}$ and $I_{litter}^{bg,h}$). These values for corn and soybean are summarized and incorporated by Woo et al. (2014; Table 1).

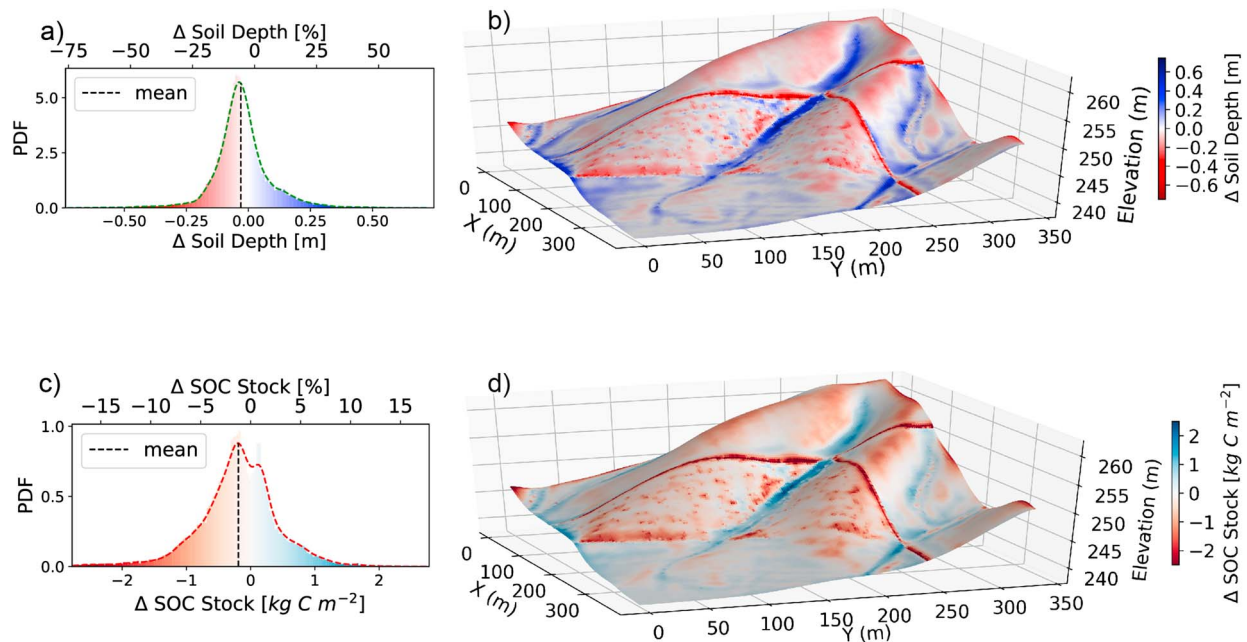


Figure 8. Simulation results for soil depth and carbon stock changes across the subcatchment in Clear Creek Watershed and the corresponding PDFs. (a) The PDF of soil depth change (final minus initial) of each grid. The spatially mean value is -3.36×10^{-2} [m/100 years]. Positive values (blue color) represent deposition, while negative values represent erosion. The percentage value is the ratio of the depth change to the initial soil depth. (b) Spatial map of the total soil depth difference. The color is consistent with the color in (a). (c) The PDF of the total SOC change of each grid (final minus initial). The spatially mean value is -1.9×10^{-1} [kg C/m²/100 years]. The SOC stock is the vertical integration of SOC concentration in each soil column in the computational grid. (d) Spatial map of the total SOC stock change. The color is consistent with the color in (c). SOC = soil organic carbon; PDF = probability distribution function.

4. Results

The model outputs include the SOC concentration profile, surface water depth, soil moisture, surface elevation, and soil thickness with a 2-m horizontal resolution at a daily time step (Table 2). Here we focus on four aspects—the SOC stock change, SOC vertical profile, the relationship between physical transport and the biogeochemical transformation of SOC, and the impacts of mechanical soil mixing from agricultural tillage on SOC stock change. The initial SOC profile is estimated as an exponential profile (Harden et al., 1999) and follows the trend of the observation profiles below the nose (Figure 6d). The initial soil thickness is specified as 1 m with seven layers (see the thickness of each layer in Table 2). Both the SOC profile and soil thickness are the same at each grid box at time zero.

4.1. Spatial Distribution of SOC Stock Changes

To explore the evolution of elevation (or soil thickness) and SOC stock, we plot the final results after a 100-year simulation (Figure 8). The results show the difference between the final and initial values. Figures 8a and 8b show the soil depth change over 100 years. Since the uplift rate is 0, the topography, in general, is decaying. The spatially mean value of soil thickness change rate is -3.36×10^{-4} [m/year], which is in the same range of magnitude as the results provided by Abaci and Papanicolaou (2009) and Brantley et al. (2015) for the IML-CZO. Surface soils are removed from the ridges and deposited into the low-lying area. The highest deposition zone is in the center of this subcatchment (a grass waterway), while the most severe erosion zone is on the ridges and the edges of high gradient areas. One noticeable red band (severe erosion zone) from left to right across the domain in Figure 8b is a grass strip with higher local relief. However, the width of the grass strip is within 2 m, which is only one grid point on the simulation domain. Therefore, the impact of the erosion from the red band on the probability density function (PDF) of the entire domain (Figure 8a) is relatively small.

We obtain the SOC stock for each grid by integrating the SOC concentration over the soil depth in the simulation. The SOC stock change (Figures 8c and 8d) generally follow the patterns of soil depth change. The spatially mean value of the net SOC stock change rate is -1.9 [g C/m²/year], which is within the same range of magnitude estimated by Papanicolaou et al. (2015). The shape of the PDF (Figure 8c) of the SOC

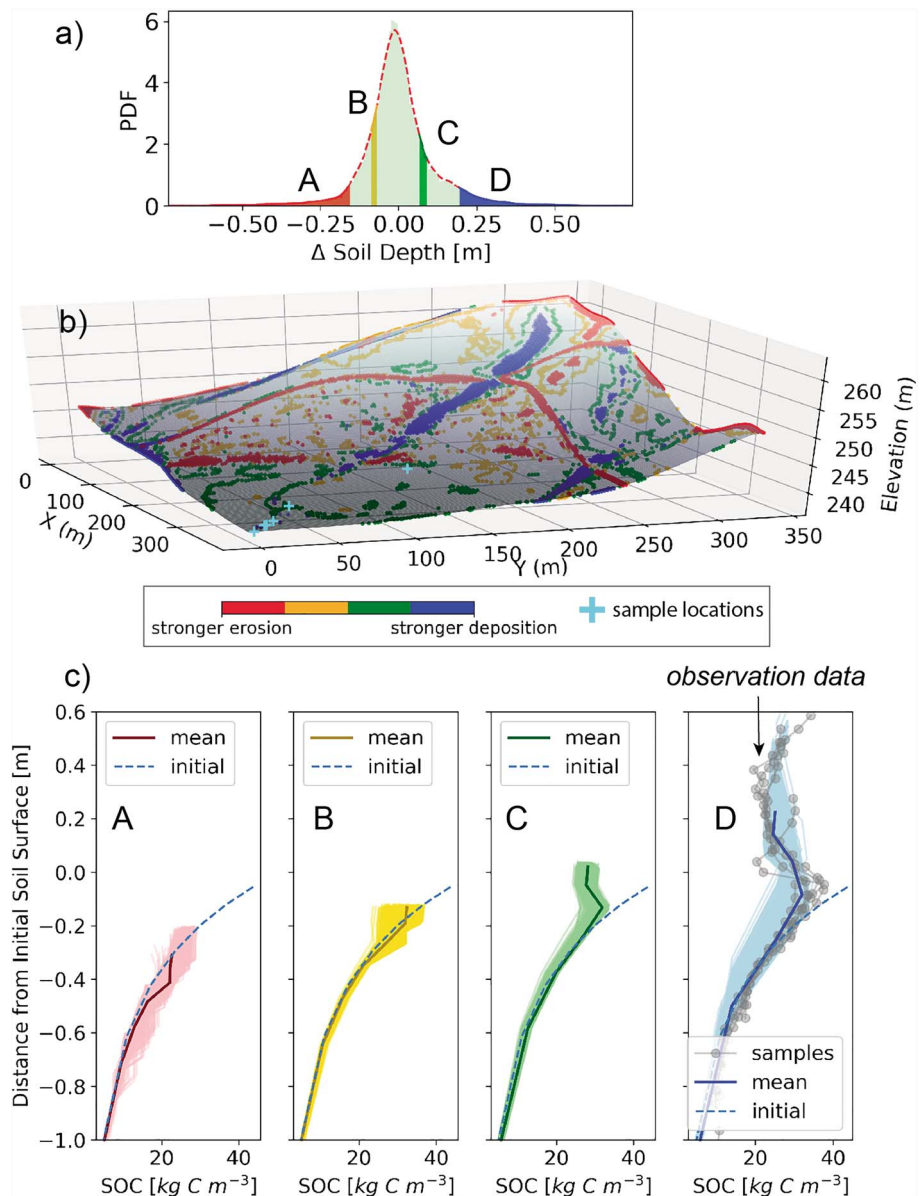


Figure 9. Comparison of simulated and observed (samples) SOC profiles. (a) PDF of soil depth change (at the end of 100-year minus the initial depth). The four colored bands, A–D, are four zones (representing 5% each with profiles B and C anchored at twentieth and eightieth percentiles) ranging from strong erosion (Zone A, red), erosion (Zone B, orange), deposition (Zone C, green), to strong deposition (Zone D, blue). (b) The spatial locations corresponding to the four zones. (c) The corresponding vertical concentration profiles of SOC of the four zones. The light colors (pink, yellow, green, and blue) are profiles of each grid point. The corresponding darker lines are the mean SOC concentration profile of each zone. The grid and dotted lines overlapping with Zone D are the sampling data. SOC = soil organic carbon; PDF = probability distribution function.

stock change is quite different from the one of soil depth. The standard deviations for the percentage of SOC stock and soil thickness change are 4.0 and 11.5, respectively. This difference is due to the effect of biogeochemical transformation because SOC change is a result of the combination of soil thickness change and biogeochemical transformation. The detailed explanations of the evolution of SOC can be found in the following subsections.

4.2. SOC Vertical Profile and Model Validation

To explore the spatial distribution of SOC profiles, we choose four distinct zones from the PDF of soil depth change (Figure 9a), which represents different ranges of the segments in the study area. A–D in the PDF

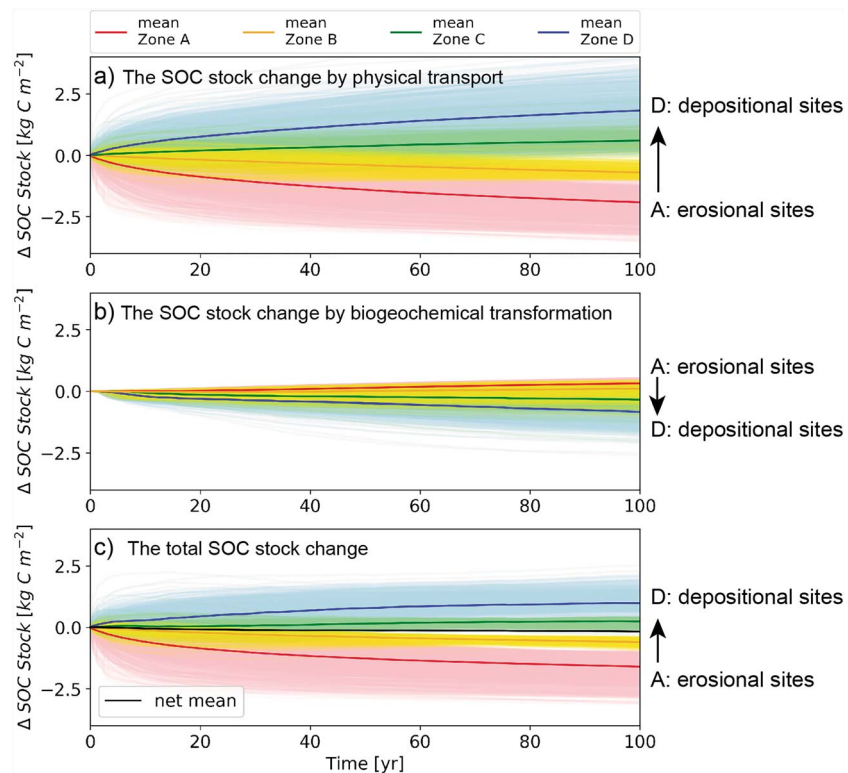


Figure 10. C stock change on each grid as simulation progress through 100 years for each of the four zones shown in Figure 9. (a) The SOC stock change due to the lateral physical transport. (b) The SOC stock change due to biogeochemical transformation and (c) total SOC stock change, which is the sum of (a) and (b). Positive and negative values indicate gain and loss, respectively. Each light colored line corresponds to a grid on the surface and the corresponding darker/highlighted line is the mean value for each zone. The black line in (c) is the total spatial (net) mean value. SOC = soil organic carbon.

represent the soil depth change from the most severe erosion zone (A, red color) to the highest deposition zone (D, blue color). The topography (Figure 9b) is recolored using the corresponding colors of each zone. The stronger deposition zones are mostly in the center of a grass pathway, and stronger erosion zones are in the uplands and areas that divide farmlands (red band in Figure 9b). Erosion and deposition are scattered spatially. The SOC profiles (Figure 9c) are from each of the recolored grid.

In order to capture the impact of tillage from agriculture, we simulated additional 10-year of coevolution by applying mechanical mixing of the top 20-cm soil (see details of mechanical soil mixing in section 4.4). The reason is that based on the USDA crop cover database, the six sampling sites are converted from natural shrubs or trees to crop land within the past 10 years. Applying a 10-year mechanical mixing of SOC helps to compare the simulated SOC profiles with the sampling results and evaluate the model's performance.

Figure 9c shows the vertical carbon concentration profiles of the four zones. The dashed line is the specified initial SOC profile. The light colors represent the profile at each grid in the respective zones, and the relatively darker color is the mean value in each zone. At the erosion sites (Zones A and B), the soil thickness become thinner as expected. The SOC at the newly exposed surface, however, increases compared to the original value due to the accumulation of new carbon by dynamic replacement (Harden et al., 1999). Even though the net gain of SOC from plant residues does not fully compensate the loss due to erosion, the rate of SOC decomposition is slower than gain from residues. This indicates that the erosional sites could favor C sequestration by providing a local net sink of atmospheric C consistent with other studies (Doetterl et al., 2016; Quinton et al., 2010; Van Oost et al., 2007). We explore more about the relationship between SOC transport and biogeochemical transformation in section 4.3.

At the depositional sites (Figure 9c; Zones C and D), during the early stage of fast erosion and deposition, the preagriculture soils with relatively high carbon concentration from erosional sites are buried below the surface resulting in reduced decomposition rate. Over time, the SOC concentrations transported from erosional

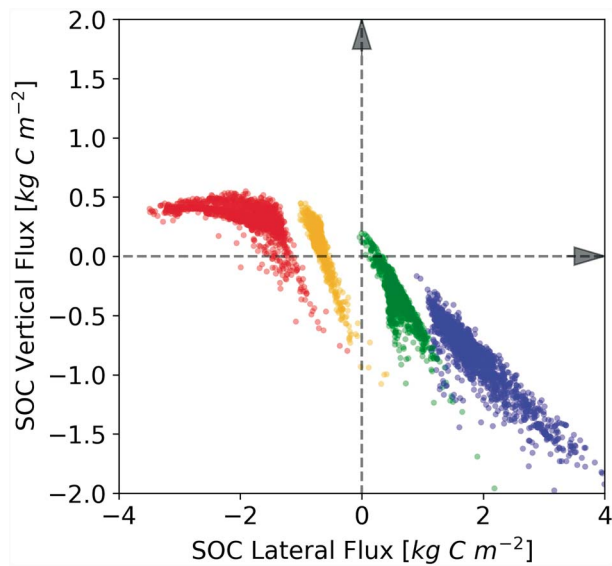


Figure 11. Relationships between the accumulated lateral and vertical carbon flux at the end of the 100-year simulation. The four colors correspond to the four zones (5%) in Figure 9a. The accumulated carbon flux is same as the SOC stock change. A positive value for lateral flux means more SOC is deposited than eroded on that grid. A positive value for vertical flux means the rate of SOC accumulation is higher than decomposition. Most of the depositional sites have negative vertical flux, indicating they are local atmospheric C source, while most of the erosional sites have positive vertical flux, indicating local atmospheric carbon sink. SOC = soil organic carbon.

to depositional sites become lower because they come from a deeper soil layer with lower SOC concentrations. Consequently, this process leaves the depositional sites with relatively lower carbon concentrations on the surface than belowground. This eventually leaves a nose on the profile. At the same time, the biogeochemical transformation has an impact on the profile, even though it is not as significant as the SOC transport. Once the new SOC deposits, the rate of SOC decomposition rate is fast, so the deposited SOC concentration decreases fast in the early stage. However, with the SOC being rapidly buried deeper, the decomposition rate slows down. That is why the SOC concentrations around the nose area are lower than the initial values (Figure 9c; Zone D). Data from the six sampling cores (Figure 6) are overlaid with the profiles in Zone D (Figure 9c). The results from sampled cores are solid lines with dots in gray color. The observed profiles match well with the simulated profiles in general, which provides a validation for the model.

4.3. Physical Transport and Biogeochemical Transformation of SOC

To compare the SOC dynamics resulting from transport and biogeochemical transformation separately, we distinguish the SOC stock changes caused by the two mechanisms. The net change of SOC by transformation represents a vertical carbon flux of soil-atmosphere exchange. This is because the vertical net exchange to the outside of soil system is an outcome of the competition between SOC decomposition (releasing atmospheric carbon) and accumulation (from plant residues). The spatial transport is a physical movement of SOC, which does not exchange carbon with atmosphere directly but changes the magnitude and turnover rate of SOC in the biogeochemical transformation process.

Figure 10 shows time series of accumulated SOC stock change by transport and transformation starting from the initial condition. Each color corresponds to the zones in Figure 9a. The spatial mean values of each zone (in darker color) are also plotted in the figure. Figures 10a and 10b show carbon stock changes caused by the SOC transport and SOC transformation, respectively. In Figure 10a the erosional sites (red and orange lines) keep losing SOC, while the depositional sites (blue and green lines) keep gaining SOC. The transformation (Figure 10b) shows the trends opposite to that of transport on SOC stocks. For example, at the erosional sites (red lines), the transformation mostly shows positive values, which means SOC decomposition rate is slower than SOC gain from plant residues. This implies that erosional sites mostly act as carbon sink to the atmospheric CO₂, and similarly, depositional sites mostly act as carbon source. In general, the total SOC stock change (Figure 10c) is consistent with the one directly redistributed by SOC transport (Figure 10a), which means the lateral transport of SOC is the dominant process in controlling the SOC stocks.

To further explore the relationship of accumulated flux between SOC transport by soil erosion/deposition (SOC lateral flux) and SOC transformation by decomposition/accumulation (SOC vertical flux), we plot the final values at the end of 100-year of simulation (Figure 11). The x axis is the SOC lateral flux—positive

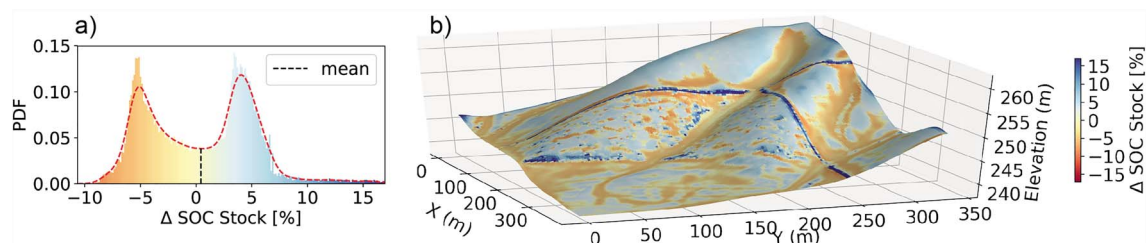


Figure 12. SOC stock difference with and without mechanical mixing. (a) The PDF of the relative SOC stock difference of mechanical mixing compared to no mechanical mixing (i.e., $\frac{\text{mechanical mixing} - \text{no mechanical mixing}}{\text{no mechanical mixing}}$). The spatially mean value is 0.4%. (b) The spatial distribution of the relative SOC stock change. PDF = probability density function; SOC = soil organic carbon.

value means gaining SOC (deposition), and negative value means losing SOC (erosion). The y axis is the SOC vertical flux—positive value means gaining SOC (decomposition is slower than plant residue input, resulting in a C sink of the atmospheric CO₂); negative value means losing SOC (decomposition is faster than plant residue input, resulting in a C source of the atmospheric CO₂). The four colors correspond to the four zones: A–D in Figure 10. In general, the lateral flux and vertical flux have opposite trend. However, on the extreme negative SOC lateral fluxes (SOC erosion, in red), the vertical fluxes (CO₂ sink) reaches an upper threshold and decreases a bit as the negative lateral fluxes are stronger. This implies an upper limit for the CO₂ sink at SOC erosional sites. Meanwhile, it is not always necessary that negative lateral flux (SOC erosion) corresponds to positive vertical flux (CO₂ sink), and vice versa. There are a few exceptions. At some locations (green dots), positive lateral transport (SOC deposition) corresponds to positive vertical flux (CO₂ sink). At other locations (red and yellow dots), negative lateral transport (SOC erosion) corresponds to negative vertical flux (CO₂ source). These “exceptions” take place with relatively small SOC lateral flux. One possible reason would be that since the net lateral flux equals the incoming flux subtracted by outgoing flux, a negative net lateral flux (SOC erosion) also has impact from incoming flux, particularly, when the magnitudes of incoming and outgoing flux are comparable.

4.4. Impact of Tillage on SOC Cycles

To compare the impacts of mechanical mixing, we run the model twice. One run is a 100-year simulation without mechanical mixing, and the second run uses the same input but includes the mechanical mixing at day 105 of each year. Here we assume the mechanical mixing tills the top 20-cm soils in this subcatchment (Papanicolaou et al., 2015), and the two runs share the same soil erodibility.

Figure 12 shows the relative SOC stock difference (mechanical mixing minus nonmechanical mixing) and then divided by nonmechanical mixing) between the two. The mechanical mixing here only change the shapes of SOC profiles (see Figure 3), which affect the biogeochemical transformation but not the lateral transport. The mechanical mixing favors the SOC stock stored in the landscape with the net mean value of 0.4% more compared to nonmechanical mixing. The relative SOC stock difference is within 17% but shows a clear spatial pattern. At erosional sites, the SOC stock is higher with mechanical than nonmechanical mixing and vice versa at depositional sites. The results show that mechanical mixing would enhance the SOC stock at erosional sites but reduce the SOC stock at depositional sites. The reasons is that mechanical mixing homogenizes the top SOC concentration. At erosional sites, the surface SOC concentrations are reduced (Figure 3a), which exposes subsoil, slows down the decomposition rate, and hence favors the SOC storage near the surface; meanwhile below-surface SOC concentrations are increased because mechanical mixing buries more SOC belowground. Similarly, at depositional sites, before mechanical mixing, the surface SOC concentration would be lower than near surface (Figure 3b), then the results are opposite as the erosional sites.

5. Discussion

The quasi 3-D model, SCALE, we have developed is, for the first time, capable of simulating the coevolution of landscape and SOC profiles and stocks in a watershed scale with fine temporal and spacial resolutions. The model resolves SOC dynamics along soil depth to simulate the evolution of SOC concentration profile as well as SOC stock. One advantage of this model is that it allows us to disentangle the impacts of surface lateral transport (and resultant landscape evolution) and biogeochemical transformation. Another advantage is that the model is capable of incorporating other variations and processes. For example, the soil weathering rate can be included in the soil thickness relationship (equation (16)); the value of glacial rebound or tectonic uplift rate can be included in equation (10); influence of aggregates can be considered on soil erosion/deposition flux (equations (14) and (15)) as well as the biogeochemical transformation (equation (7)).

The modeling results show that the SOC profiles and stocks are heterogenous across landscapes (Figures 6 and 9). For example, at erosional sites, the profiles are exponentially decreasing except for the tillage depth, and at depositional sites, the SOC profiles have a nose mainly from SOC accumulation from lateral transport. In a relatively fast erosion landscape, the SOC lateral transport (led by soil transport) is a dominant control on the SOC stock change (Figure 8). The lateral transport of SOC is a physical movement on the soil surface and does not exchange C with atmosphere directly; while the biogeochemical transformation

involves decomposing (releasing CO_2) and accumulating SOC from plant residues (sequestering CO_2), so it represents the vertical C exchange between soil and atmosphere.

The simulation results show that the majority of the erosional sites are net local atmospheric C sink (which means the rate of gain of SOC from plant residues is higher than metabolic losses as CO_2), and the majority of the depositional sites are net local atmospheric C source (Figures 10 and 11). At erosional sites, lateral SOC flux leads to an exposure of subsoil. SOC inventories may increase within the newly exposed soil because exposing the formerly deep soils would increase the amount of reactive soil minerals that binds organic matter. Hence, this biogeochemical transformation of eroded SOC (SOC vertical flux) could provide a local net sink of atmospheric C (Doetterl et al., 2016; Quinton et al., 2010; Van Oost et al., 2007). However, exception are drawn out from our simulation results that exposure of subsoil leads to a local net source, instead of sink, of atmospheric CO_2 (Figure 11). This is consistent with other field observations (Doetterl et al., 2016; Lal, 2004; Quinton et al., 2010). At depositional sites, former top soil layers with relative high SOC content are gradually buried into deeper layers. The burial suppresses aerobic decomposition rate, but the total amount of decomposed SOC would increase because of the increased availability of SOC. In our study area, the burial of SOC mostly results in a net source of atmospheric CO_2 (Figure 11). Our results show that the magnitude of vertical flux of soil-atmosphere C exchange could be as high as 3 times than the vertical flux at erosional sites. Van Oost et al. (2007) found the flux at depositional sites, however, has a smaller magnitude than the flux at erosional sites. Overall, these different combinations between SOC lateral (erosion and deposition) and vertical fluxes (soil-atmosphere C exchange) would depend on microtopography and seasonal meteorology forcings. This provides a hint for potential C hotspots on a landscape and will be pursued as a research focus in the future.

6. Conclusion

We built a process-based modeling framework, SCALE, that synthesizes aboveground and belowground processes, including landscape evolution, surface water runoff, organic matter transformation, and soil moisture dynamics to understand the coevolution of landscape and the SOC dynamics in a watershed scale in a fine spatial and temporal resolution. This model provides a depth-resolved simulation of SOC cycle, which captures the evolution of SOC profiles and stocks. We applied this model to a subcatchment in the CCW in Iowa. It shows that in an agricultural landscape (e.g., corn and soybean rotation) the SOC physical transport rather than the biogeochemical transformation is dominant on SOC profiles as well as the stocks. Also, the SOC profiles are heterogeneous. At erosional sites, the SOC concentrations are exponentially declining along soil depth except for the near-surface tillage zone where the profiles are close to a uniform shape. At depositional sites, the vertical profiles have a nose below the surface mainly caused by burial of legacy SOC. The model is not calibrated with the observed data, but the simulation results are validated and consistent with the findings from cores sampled at the same study site. The biogeochemical transformation shows opposite behaviors at erosional and depositional sites. In most of the cases, the rate of SOC decomposition is slower than gain from plant residues at an erosional site, which serves as a net atmospheric C sink, and vice versa for a depositional site, which is generally a net C source. Exceptions are drawn out in a few cases that erosional sites serve as net atmospheric C source, and depositional sites serve as net C sink. The mechanical mixing as one direct outcome of tillage would increase the SOC stock at erosional sites and reduce the stock at depositional sites. This study not only helps us understand the SOC stocks and fluxes but could also serve as an instrument to develop practical means for protecting carbon loss by human activities.

References

- Abaci, O., & Papanicolaou, A. N. T. (2009). Long-term effects of management practices on water-driven soil erosion in an intense agricultural sub-watershed: Monitoring and modelling. *Hydrological Processes*, 23(November 2008), 2818–2837. <https://doi.org/10.1002/hyp.7380>
- Amenu, G. G., & Kumar, P. (2008). A model for hydraulic redistribution incorporating coupled soil-root moisture transport. *Hydrology and Earth System Sciences Discussions*, 12(1), 55–74. <https://doi.org/10.5194/hess-12-55-2008>
- Amundson, R., Berhe, A. A., Hopmans, J. W., Olson, C., Szein, A. E., & Sparks, D. L. (2015). Soil and human security in the 21st century. *Science*, 348(6235), 1261071. <https://doi.org/10.1126/science.1261071>
- Berhe, A. A., Harden, J. W., Torn, M. S., & Harte, J. (2008). Linking soil organic matter dynamics and erosion-induced terrestrial carbon sequestration at different landform positions. *Journal of Geophysical Research*, 113, G04039. <https://doi.org/10.1029/2008JG000751>
- Berhe, A. A., Harte, J., Harden, J. W., & Torn, M. S. (2007). The significance of the erosion-induced terrestrial carbon sink. *BioScience*, 57(4), 337–346. <https://doi.org/10.1641/B570408>

Acknowledgments

Funding support from National Science Foundation Grants EAR 1331906 (Intensively Managed Landscapes Critical Zone Observatory, IML-CZO) and CBET 1290445, ACI 1261582 (BrownDog) are gratefully acknowledged. We also acknowledge Alison Anders and Asmeret Berhe for insightful discussions. Thanks to Debsunder Dutta for his help on processing Landsat data set. We also thank Ming Li and Ulyssa Hester for assistance in the laboratory processing of the soil core samples. Thanks to the workshop, “Mathematical Modeling of Earth’s Dynamic Systems,” hosted at Penn State in Summer 2016 for its travel grant to Qina Yan. The authors declare no conflict of interest. The Landsat 7 ETM+ C1 Level-1 data product was retrieved from the online Data Pool, courtesy of the NASA Land Processes Distributed Active Archive Center (LP DAAC), USGS/Earth Resources Observation and Science (EROS) Center, Sioux Falls, South Dakota, <https://earthexplorer.usgs.gov/>. The 10-year recorded meteorological data were retrieved from weather underground, <https://www.wunderground.com/weather/us/ia/iowa-city/>. Data of LiDAR DEM and soil core samples used in this research are openly available at <https://github.com/HydroComplexity/SCALE>.

- Berhe, A. A., & Torn, M. S. (2017). Erosional redistribution of topsoil controls soil nitrogen dynamics. *Biogeochemistry*, 132(1-2), 37–54. <https://doi.org/10.1007/s10533-016-0286-5>
- Billings, S. A., Buddemeier, R. W., De, D., Van Oost, K., & Bohling, G. (2010). A simple method for estimating the influence of eroding soil profiles on atmospheric CO₂. *Global Biogeochemical Cycles*, 24, GB2001. <https://doi.org/10.1029/2009GB003560>
- Borrelli, P., Robinson, D. A., Fleischer, L. R., Lugato, E., Ballabio, C., Alewell, C., et al. (2017). An assessment of the global impact of 21st century land use change on soil erosion. *Nature Communications*, 8(1). <https://doi.org/10.1038/s41467-017-02142-7>
- Brady, N., & Weil, R. (1996). *The nature and properties of soils* (11th ed.). Upper Saddle River, NJ: Prentice Hall.
- Brantley, S. L., Dietrich, W. E., & Banwart, S. (2015). An international initiative for science in the critical zone. *EOS*, 96. <https://doi.org/10.1029/2015EO031111>
- Camporese, M., Daly, E., Dresel, P. E., & Webb, J. A. (2014). Simplified modeling of catchment-scale evapotranspiration via boundary condition switching. *Advances in Water Resources*, 69, 95–105. <https://doi.org/10.1016/j.advwatres.2014.04.008>
- Camporese, M., Paniconi, C., Putti, M., & Orlandini, S. (2010). Surface-subsurface flow modeling with path-based runoff routing, boundary condition-based coupling, and assimilation of multisource observation data. *Water Resources Research*, 46, W02512. <https://doi.org/10.1029/2008WR007536>
- Celia, M. A., Bouloutas, E. T., & Zarba, R. L. (1990). A general mass conservative numerical solution for the unsaturated flow equation. *Water Resources Research*, 26(1), 1483–1496. <https://doi.org/10.1029/WR026i007p01483>
- Clapp, R. B., & Hornberger, G. M. (1978). Empirical equations for some soil hydraulic properties. *Water Resources Research*, 14(4), 601–604. <https://doi.org/10.1029/WR014i004p0601>
- Clement, T. P., Wise, W. R., & Molz, F. J. (1994). A physically based, two-dimensional, finite-difference algorithm for modeling variably saturated flow. *Journal of Hydrology*, 161(1-4), 71–90. [https://doi.org/10.1016/0022-1694\(94\)90121-X](https://doi.org/10.1016/0022-1694(94)90121-X)
- Culling, W. E. H. (1960). Analytical theory of erosion. *The Journal of Geology*, 68(3), 336–344.
- Danalatos, N., Kosmas, C., Driessen, P., & Yassoglou, N. (1994). The change in the specific leaf area of maize grown under Mediterranean conditions. *Agronomie*, 14, 433–443. <https://doi.org/10.1051/agro:19940702>
- David, M. B., McIsaac, G. F., Darmody, R. G., & Omonode, R. A. (2009). Long-term changes in mollisol organic carbon and nitrogen. *Journal of Environment Quality*, 38(1), 200. <https://doi.org/10.2134/jeq2008.0132>
- Dialynas, Y. G., Bastola, S., Bras, R. L., Billings, S. A., Markewitz, D., & Richter, D. d. (2016). Global biogeochemical cycles of soil erosion on the carbon cycle. *Global Biogeochemical Cycles*, 30, 644–660. <https://doi.org/10.1002/2015GB005302>
- Dietrich, W. E., Bellugi, D. G., Heimsath, A. M., Roering, J. J., Sklar, L. S., & Stock, J. D. (2003). Geomorphic transport laws for predicting landscape form and dynamics. *Geophysical Monograph*, 135(D24), 1–30. <https://doi.org/10.1029/135GM09>
- Dlugoß, V., Fiener, P., Van Oost, K., & Schneider, K. (2012). Model based analysis of lateral and vertical soil carbon fluxes induced by soil redistribution processes in a small agricultural catchment. *Earth Surface Processes and Landforms*, 37(2), 193–208. <https://doi.org/10.1002/esp.2246>
- Doetterl, S., Asefaw, A., Nadeu, E., Wang, Z., Sommer, M., & Fiener, P. (2016). Erosion, deposition and soil carbon: A review of process-level controls, experimental tools and models to address C cycling in dynamic landscapes. *Earth Science Reviews*, 154, 102–122. <https://doi.org/10.1016/j.earscirev.2015.12.005>
- Fan, J., & Hou, X. (2016). International stratigraphic chart.
- Fernandes, N. F., & Dietrich, W. E. (1997). Hillslope evolution by diffusive processes: The timescale for equilibrium adjustments. *Water Resources Research*, 33(6), 1307–1318. <https://doi.org/10.1029/97WR00534>
- Finke, P. A., & Hutson, J. L. (2008). Modelling soil genesis in calcareous loess. *Geoderma*, 145(3-4), 462–479. <https://doi.org/10.1016/j.geoderma.2008.01.017>
- Foster, G. R., Flanagan, D. C., Nearing, M. A., Lane, L. J., Risse, L. M., & Finkner, S. C. (1995). Hillslope erosion component, in USDA-water erosion prediction project: Hillslope profile and watershed model documentation. West Lafayette, IN: National Soil Erosion Research Lab.
- Furbish, D. J., & Fagherazzi, S. (2001). Stability of creeping soil and implications for hillslope evolution. *Water Resources Research*, 37(10), 2607–2618.
- Hanway, J. J. (1966). How a corn plant develops. Iowa: Iowa State University Cooperative Extension Service Special Report 38.
- Hanway, J. J., & Thompson, H. E. (1967). How a soybean plant develops. Iowa: Iowa State University Cooperative Extension Service Special Report 53.
- Harden, J. W., Sharpe, J. M., Parton, W. J., Ojima, D. S., Fries, T. L., Huntington, T. G., & Dabney, S. M. (1999). Dynamic replacement and loss of soil carbon on eroding cropland. *Global Biogeochemical Cycles*, 13(4), 885–901. <https://doi.org/10.1029/1999GB000061>
- Hendrix, P. F., Han, C. R., & Groffman, P. M. (1988). Soil respiration in conventional and no-tillage agroecosystems under different winter cover crop rotations. *Soil and Tillage Research*, 12(2), 135–148. [https://doi.org/10.1016/0167-1987\(88\)90037-2](https://doi.org/10.1016/0167-1987(88)90037-2)
- Hopkins, F. M., Filley, T. R., Gleixner, G., Lange, M., Top, S. M., & Trumbore, S. E. (2014). Increased belowground carbon inputs and warming promote loss of soil organic carbon through complementary microbial responses. *Soil Biology and Biochemistry*, 76, 57–69. <https://doi.org/10.1016/j.soilbio.2014.04.028>
- Howard, A. D., & Kerby, D. (1893). Channel changes in badlands. *Geological Society of America Bulletin*, 94(6), 739–752. [https://doi.org/10.1130/0016-7606\(1983\)94<739:CCIB>2.0.CO;2](https://doi.org/10.1130/0016-7606(1983)94<739:CCIB>2.0.CO;2)
- Ito, A. (2007). Simulated impacts of climate and land-cover change on soil erosion and implication for the carbon cycle, 1901 to 2100. *Geophysical Research Letters*, 34, L09403. <https://doi.org/10.1029/2007GL029342>
- Ivanov, V. Y., Bras, R. L., & Curtis, D. C. (2007). A weather generator for hydrological, ecological, and agricultural applications. *Water resources research*, 43, W10406. <https://doi.org/10.1029/2006WR005364>
- Julien, P. Y., & Simons, D. B. (1985). *Sediment transport capacity of overland flow*. Michigan: American Society of Agricultural and Biological Engineers. <https://doi.org/10.13031/2013.32333>
- Kilinc, M., & Richardson, E. V. (1973). *Mechanics of soil erosion from overland flow generated by simulated rainfall* (pp. 63). Fort Collins: Hydrology Papers.
- Kumar, P., Le, P. V. V., Papanicolaou, A. N. T., Rhoads, B. L., Anders, A. M., Stumpf, A., et al. (2018). Critical transition in critical zone of intensively managed landscapes. *Anthropocene*, 22(2213-3054), 10–19. <https://doi.org/10.1016/j.jancene.2018.04.002>
- Lal, A. M. W. (1998). Performance comparison of overland flow algorithms. *Journal of Hydraulic Engineering*, 124(4), 342–349. [https://doi.org/10.1061/\(ASCE\)0733-9429\(1998\)124:4\(342\)](https://doi.org/10.1061/(ASCE)0733-9429(1998)124:4(342))
- Lal, R. (2004). Soil carbon sequestration to mitigate climate change. *Geoderma*, 123(1-2), 1–22. <https://doi.org/10.1016/j.geoderma.2004.01.032>
- Lal, R. (2008). Sequestration of atmospheric CO₂ in global carbon pools. *Energy & Environmental Science*, 1(1), 86. <https://doi.org/10.1039/b809492f>

- Latshaw, W. L., & Miller, E. C. (1924). Elemental composition of the corn plant. *Journal of Agricultural Research*, 27(11), 845–861.
- Le, P. V., & Kumar, P. (2017). Interaction between ecohydrologic dynamics and microtopographic variability under climate change. *Water Resources Research*, 53, 8383–8403. <https://doi.org/10.1002/2017WR020377>
- Le, P. V. V., Kumar, P., Valocchi, A. J., & Dang, H. V. (2015). GPU-based high-performance computing for integrated surface-sub-surface flow modeling. *Environmental Modelling and Software*, 73, 1–13. <https://doi.org/10.1016/j.envsoft.2015.07.015>
- Lehmann, J., & Kleber, M. (2015). The contentious nature of soil organic matter. *Nature*, 528(7580), 60–68. <https://doi.org/10.1038/nature16069>
- Li, C., Frolking, S., & Harriss, R. (1994). Modeling carbon biogeochemistry in agricultural soils. *Global Biogeochemical Cycles*, 8(3), 237–254. <https://doi.org/10.1029/94GB00767>
- Liu, S. (2003). Modeling carbon dynamics in vegetation and soil under the impact of soil erosion and deposition. *Global Biogeochemical Cycles*, 17(2), 1074. <https://doi.org/10.1029/2002GB002010>
- Montgomery, D. R. (2007). Soil erosion and agricultural sustainability. *Proceedings of the National Academy of Sciences of the United States of America*, 104(33), 13,268–13,272. <https://doi.org/10.1073/pnas.0611508104>
- Nguy-Robertson, A., Gitelson, A., Peng, Y., Viña, A., Arkebauer, T., & Rundquist, D. (2012). Green leaf area index estimation in maize and soybean: Combining vegetation indices to achieve maximal sensitivity. *Agronomy Journal*, 104(5), 1336–1347. <https://doi.org/10.2134/agronj2012.0065>
- O'dorico, P., Laio, F., Porporato, A., & Rodriguez-Iturbe, I. (2003). Hydrologic controls on soil carbon and nitrogen cycles. II. A case study. *Advances in Water Resources*, 26, 59–70.
- Paniconi, C., & Wood, E. F. (1993). A detailed model for simulation of catchment scale subsurface hydrologic processes. *Water Resources Research*, 29(6), 1601–1620. <https://doi.org/10.1029/92WR02333>
- Papanicolaou, A., Wacha, K. M., Abban, B. K., Wilson, C. G., Hatfield, J. L., Stanier, C. O., & Filley, T. R. (2015). From soils to landscapes: A landscape-oriented approach to simulate soil organic carbon dynamics in intensively managed landscapes. *Journal of Geophysical Research: Biogeosciences*, 120, 979–988. <https://doi.org/10.1002/2014JG002802>. Received
- Pelletier, J. D. (2011). Fluvial and slope-wash erosion of soil-mantled landscapes: Detachment- or transport-limited? *Earth Surface Processes and Landforms*, 37(1), 37–51. <https://doi.org/10.1002/esp.2187>
- Perron, J. T. (2011). Numerical methods for nonlinear hillslope transport laws. *Journal of Geophysical Research*, 116, F02021. <https://doi.org/10.1029/2010JF001801>
- Porporato, A., O'dorico, P., Laio, F., & Rodriguez-Iturbe, I. (2003). Hydrologic controls on soil carbon and nitrogen cycles. I. Modeling scheme. *Advances in Water Resources*, 26(1), 45–58. [https://doi.org/10.1016/S0309-1708\(02\)00094-5](https://doi.org/10.1016/S0309-1708(02)00094-5)
- Potter, S. R., Andrews, S., Atwood, J. D., Kellogg, R. L., Lemunyon, J., Norfleet, L., & Oman, D. (2006). Model simulation of soil loss, nutrient loss, and change in soil organic carbon associated with crop production. Washington, DC: Natural Resources Conservation Service.
- Prosser, I. P., & Rustomji, P. (2000). Sediment transport capacity relations for overland flow. *Progress in Physical Geography*, 24(2), 179–193. <https://doi.org/10.1177/030913330002400202>
- Quijano, J. C., Kumar, P., & Drewry, D. T. (2013). Passive regulation of soil biogeochemical cycling by root water transport. *Water Resources Research*, 49, 3729–3746. <https://doi.org/10.1002/wrcr.20310>
- Quinton, J. N., Govers, G., Oost, K. V., & Bardgett, R. D. (2010). The impact of agricultural soil erosion on biogeochemical cycling. *Nature Geoscience*, 3(10), 311–314. <https://doi.org/10.1038/NGEO838>
- Richards, L. A. (1931). Capillary conduction of liquids through porous mediums. *Journal of Applied Physics*, 1(5), 318–333. <https://doi.org/10.1063/1.1745010>
- Scott, H. D., & Batchelor, J. T. (1979). Dry weight and leaf area production rates of irrigated determinate soybeans. *Agronomy Journal*, 71, 776–782.
- Smith, S., Renwick, W., Buddemeier, R. W., & Crossland, C. J. (2001). Budgets of soil erosion and deposition for sediments and sedimentary organic carbon across the posited across the United States. *Global Biogeochemical Cycles*, 15(3), 697–707. <https://doi.org/10.1029/2000GB001341>
- Srivastava, A. C., Tiku, A. K., & Pal, M. (2006). Nitrogen and carbon partitioning in soybean under variable nitrogen supplies and acclimation to the prolonged action of elevated CO₂. *ACTA Physiologiae Plantarum*, 28(2), 181–188. <https://doi.org/10.1007/s11738-006-0045-7>
- Stallard, R. F. (1998). Terrestrial sedimentation and the carbon cycle: Coupling weathering and erosion to carbon burial. *Global Biogeochemical Cycles*, 12(2), 231–257. <https://doi.org/10.1029/98GB00741>
- Sulis, M., Meyerhoff, S. B., Paniconi, C., Maxwell, R. M., Putti, M., & Kollet, S. J. (2010). A comparison of two physics-based numerical models for simulating surface water-groundwater interactions. *Advances in Water Resources*, 33(4), 456–467. <https://doi.org/10.1016/j.advwatres.2010.01.010>
- Temme, A. J., & Vanwalleghe, T. (2016). LORICA—A new model for linking landscape and soil profile evolution: Development and sensitivity analysis. *Computers and Geosciences*, 90, 131–143. <https://doi.org/10.1016/j.cageo.2015.08.004>
- Thompson, S. E., Katul, G. G., & Porporato, A. (2010). Role of microtopography in rainfall-runoff partitioning: An analysis using idealized geometry. *Water Resources Research*, 46, W07520. <https://doi.org/10.1029/2009WR008835>
- Van Genuchten, M. T. (1980). A closed-form equation for predicting the hydraulic conductivity of unsaturated soils. *Soil Science Society of America Journal*, 44(5), 892. <https://doi.org/10.2136/sssaj1980.03615995004400050002x>
- Van Oost, K., Govers, G., Quine, T. A., Heckrath, G., Olesen, J. E., De Gryze, S., & Merckx, R. (2005). Landscape-scale modeling of carbon cycling under the impact of soil redistribution: The role of tillage erosion. *Global Biogeochemical Cycles*, 19, GB4014. <https://doi.org/10.1029/2005GB002471>
- Van Oost, K., Quine, T. A., Govers, G., De Gryze, S., Six, J., Harden, J. W., et al. (2007). The impact of agricultural soil erosion on the global carbon cycle. *Science*, 318(5850), 626–629. <https://doi.org/10.1126/science.1145724>
- Vanwalleghe, T., Stockmann, U., Minasny, B., & Mcbratney, A. B. (2013). A quantitative model for integrating landscape evolution and soil formation. *Journal of Geophysical Research: Earth Surface*, 118, 331–347. <https://doi.org/10.1029/2011JF002296>
- Wang, X., Cammeraat, E. L. H., Romeijn, P., & Kalbitz, K. (2014). Soil organic carbon redistribution by water erosion—The role of CO₂ emissions for the carbon budget. *PLoS One*, 9(5), e96299. <https://doi.org/10.1371/journal.pone.0096299>
- Wiaux, F., Cornelis, J., Cao, W., Vanclooster, M., & Oost, K. V. (2014). Combined effect of geomorphic and pedogenic processes on the distribution of soil organic carbon quality along an eroding hillslope on loess soil. *Geoderma*, 216, 36–47. <https://doi.org/10.1016/j.geoderma.2013.10.013>
- Wieder, W. R., Bonan, G. B., & Allison, S. D. (2013). Global soil carbon projections are improved by modelling microbial processes. *Nature Climate Change*, 3(10), 909–912. <https://doi.org/10.1038/NCLIMATE1951>
- Wild, A. (1988). *Russell's soil condition and plant growth* (11th ed.). Essex, UK: Longman Group.

- Wolf, K. L., Ahn, C., & Noe, G. B. (2011). Microtopography enhances nitrogen cycling and removal in created mitigation wetlands. *Ecological Engineering*, 37(9), 1398–1046. <https://doi.org/10.1016/j.ecoleng.2011.03.013>
- Woo, D. K., Quijano, J. C., Kumar, P., Chaoka, S., & Bernacchi, C. J. (2014). Threshold dynamics in soil carbon storage for bioenergy crops. *Environmental Science & Technology*, 48(20), 12,090–12,098. <https://doi.org/10.1021/es5023762>
- Yadav, V., & Malanson, G. P. (2009). Modeling impacts of erosion and deposition on soil organic carbon in the Big Creek Basin of southern Illinois. *Geomorphology*, 106(3–4), 304–314. <https://doi.org/10.1016/j.geomorph.2008.11.011>
- Yan, Q., Iwasaki, T., Stumpf, A., Belmont, P., Parker, G., & Kumar, P. (2017). Hydrogeomorphological differentiation between floodplains and terraces. *Earth Surface Processes and Landforms*, 43(1), 218–228. <https://doi.org/10.1002/esp.4234>
- Yetemen, O., Istanbuluoglu, E., Flores-Cervantes, J. H., Vivoni, E. R., & Bras, R. L. (2015). Ecohydrologic role of solar radiation on landscape evolution. *Water Resources Research*, 51, 1127–1157. <https://doi.org/10.1002/2014WR016169>
- Zieger, A., Kaiser, K., Ríos Guayasamin, P., & Kaupenjohann, M. (2017). Massive carbon addition to an organic-rich andosol did not increase the topsoil but the subsoil carbon stock. *Biogeosciences Discussions*, 2017(November), 1–30. <https://doi.org/10.5194/bg-2017-386>

Erratum

In the originally published version of this article, Equations (20) and (22) contained typographic errors. The equations have since been corrected. The implementation of model as presented in the paper is based on these equations and not those erroneously published in the original manuscript. This version may be considered the authoritative version of record.